Review

Recent Progress in the Core-Shell Nanostructures of the NiMoO₄-Based Composite Materials for Supercapacitor Applications: A Comprehensive Review

Kandasamy Sasikumar and Heongkyu Ju *

Department of Physics, Gachon University, Seongnam-si 13120, Republic of Korea
* Correspondence: batu@gachon.ac.kr

Abstract: Supercapacitors have emerged as one of the promising energy storage systems owing to their rapid charge/discharge capability, long-term cycling stability, and high power density. The application of core-shell nanostructures for supercapacitors is one of the effective strategies to achieve a high specific surface area for abundant reaction sites and good electrical conductivity for fast charge transfer, hence improving the performance of supercapacitors. Particularly, the use of $NiMoO_4$ for the core-shell structure has drawn great attention due to its outstanding advantages, such as its natural abundance, low material cost, superior electrochemical performance, and wide electrochemical potential window in cyclic voltammetry. In this context, this review comprehensively covers the recent progress of the core-shell nanostructures based on the $NiMoO_4$-composite materials, which find applications in supercapacitors. The composite materials that incorporate metal oxides such as $NiMoO_4$, metal hydroxides, metal chalcogenides, carbon materials, and conductive polymers are discussed in detail for such core-shell nanostructures with the aim of understanding how the adopted materials and the relevant morphology govern the electrochemical features for supercapacitors. Finally, the existing challenges in current technologies for supercapacitors are discussed, while possible future directions in developing the $NiMoO_4$-composite-based core-shell nanostructures are proposed for high-performance supercapacitors.

Keywords: $NiMoO_4$; core-shell structures; morphology; supercapacitors; metal oxide; metal hydroxide; metal chalcogenide; carbon composite; conductive polymers

1. Introduction

The fast growth of the global population with industrial development demands the capability of harvesting energy more effectively with minimizing the concomitantly induced ecological hazards. Fossil fuel consumption induces environmental pollution and has increased critical concerns about global climate change as well as the ecological crisis. The International Energy Agency estimated that the energy required to be harvested from conventional fossil fuels shall rise to 18.30 billion tons of oil equivalent (btoe) in 2035 [1]. This prediction that would accelerate environmental concerns has triggered tremendous research interests in exploiting alternative and renewable energy resources, such as solar, wind, geothermal, and tidal energies, from which electricity generation has recently become somewhat effectively possible. However, most renewable energy acquisition would suffer from harvest intermittence, and it is thus crucial to develop large-scale energy storage systems to store electrical energy and offset the gap between electricity generation and energy demand.

There are many energy storage systems available, among which lithium-ion batteries and electrochemical capacitors (ECs) are at the forefront of cutting-edge technologies, as shown in the Ragone plot in Figure 1a [2]. ECs, also called supercapacitors (SCs) or ultracapacitors, occupy a unique position of having modest energy-density (0.1–10 $Whkg^{-1}$) and moderate power-density (10–10^6 Wkg^{-1}), consequently bridging the gap between batteries

(high energy-density~10–100 Whkg^{-1}; low power-density~2–200 Wkg^{-1}) and conventional capacitors (low energy-density~0.02–0.1 Whkg^{-1}; high power-density~2000–10^7 Wkg^{-1}) [2]. Over the past decade, many efforts have been devoted to SCs research because of their fascinating advantages of ultrafast charge/discharge rate, high power-density, long cyclic lifespan, high Coulombic efficiency, good safety, and low maintenance cost, with the combination of a variety of applications in consumer electronics, industrial power systems, communication systems, transportation, etc. [3]. Despite such advantages of SCs, the bottleneck that hinders their extensive use is the availability of high energy-density in SC-based devices. Therefore, boosting the energy-density without compromising the other intrinsic benefits of SCs is required. Typically, the SC is composed of a current collector, an electrode, an electrolyte, and a separator, in which the electrode material is the main factor affecting the performance of the supercapacitor.
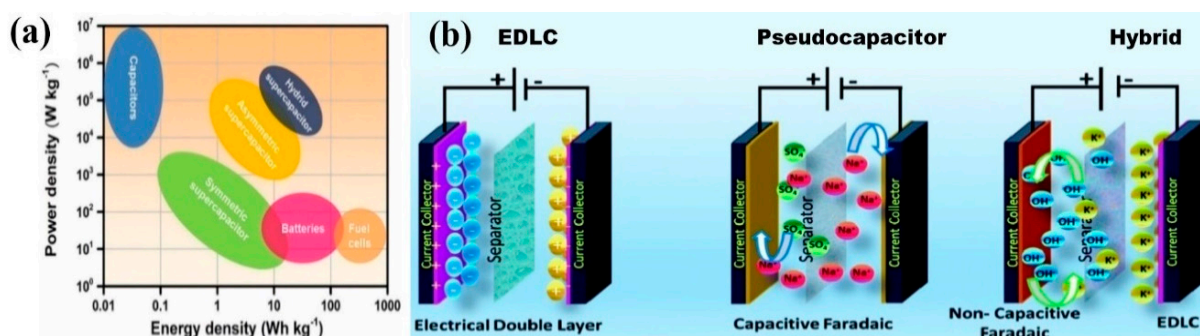

Figure 1. (**a**) Ragone plot for different electrical energy storage systems [2]. Reproduced from Ref. [2] with permission from Elsevier, 2022. (**b**) The charge storage mechanism of EDLCs, pseudocapacitors, and hybrid supercapacitors [4]. Reproduced from Ref. [4] with permission from The Royal Society of Chemistry, 2021.

Based on the energy storage mechanism, supercapacitors are basically classified into electrical double-layer capacitors (EDLCs), pseudocapacitors (PCs), and hybrid supercapacitors, as illustrated in Figure 1b [4]. The EDLCs primarily store charges through the physical adsorption and desorption of ions (non-Faradaic charge storage) taking place in the electrical double layer formed at the electrode/electrolyte interface, which leads to high power-density. Nevertheless, the low specific capacitance and energy-density hinder their widespread applications. Carbon materials, such as porous carbon, activated carbon (AC), carbon fiber, graphene, and carbon nanotube (CNT), are typically employed as electrode materials for EDLCs, owing to their good electrical conductivity, porous structure, and high surface area [5]. On the other hand, PCs store their charges by rapid and reversible electrochemical redox reactions (Faradaic charge storage) at the surface or near the surface of electroactive materials, which can provide remarkably higher specific capacitance compared to EDLCs. Therefore, in the past few years, research attempts have been made to exploit various pseudocapacitor materials, including transition metal oxides (RuO_2 and MnO_2), metal hydroxides, metal sulfides, and conductive polymers (polyaniline, polypyrrole, and polythiophene) for supercapacitor electrodes [6,7]. Meanwhile, the hybrid supercapacitor results from the combination of a high-power EDLC electrode and a high energy-density battery-type electrode (non-capacitive Faradaic charge storage).

As the materials adopted for supercapacitors, mixed transition metal oxides (MTMOs) have gained great attention because of their higher electrochemical activity, higher electrical conductivity, and multiple oxidation states than single metal oxides [8]. Recently, binary transition metal oxides (AB_xO_y) have become promising electrode materials to attain excellent supercapacitive performance. Among them, nickel molybdate ($NiMoO_4$) with spinel structure can be a potential candidate for supercapacitor application because of its intrinsic properties of high redox potential, high specific capacitance, and natural abundance-based low cost [9]. The rich redox reactions of $NiMoO_4$ are due to the multiple

valence states of nickel ion (Ni^{2+}/Ni^{3+}) mediated by OH^- ions in the alkaline electrolyte (KOH or NaOH). During the electrochemical cycle test, the charge storage on the $NiMoO_4$ electrode surface arises according to the following redox reaction [10–14],

$$Ni(OH)_2 + OH^- \Leftrightarrow NiOOH + H_2O + e^- \tag{1}$$
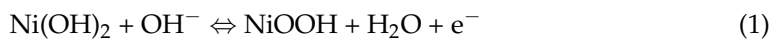
It is noted that the bulk material of $NiMoO_4$ still suffers from some issues, for example, low-rate capability and poor cycle performance caused by the dissolution of active materials during cycling tests. This problem, however, can be solved by downsizing the material from bulk to nanoscale, i.e., by synthesizing $NiMoO_4$ nanostructures [15–17]. Compared to the bulk material, the nanostructure can provide more active sites and facilitate electron transport by shortening the diffusion pathway, consequently improving rate capability and cycling stability during the charge/discharge process [18]. In addition to the downsizing benefits, the use of a combination of $NiMoO_4$ and other transition metal oxides for synthesis can result in greater electrochemical performance. Several reports are available on the core-shell structure, in which an inner "core" material is surrounded by an outer "shell" material having similar or different properties from the core [19]. The core-shell structure is designed such that the core is the active material with functional properties while the shell protects and strengthens the core to augment the supercapacitive performance. The core-shell nanostructure creates hierarchical porous channels for active charge transport and holds high electrical conductivity while maintaining better mechanical stability.

There are many articles solely reporting the development and challenges of transition metal oxides, such as MnO_2, WO_3, CuO/Cu_2O, $CuCo_2O_4$, and $NiCo_2O_4$ for supercapacitor applications [7,8,19]. The synthesis strategies, energy storage mechanisms, and electrochemical performance of these core-shell structured composites have been reviewed in detail. But the topic of core-shell structures based on $NiMoO_4$-composite materials for supercapacitors has not been reviewed so far. Moreover, compared to single metal oxides, the use of mixed transition metal oxides can result in improved electrochemical performance. Considering $NiMoO_4$, it is interesting to note that Ni and Mo ions individually contribute to redox activity and conductivity. Therefore, this article mainly focuses on the research progress made in the past decade on the core-shell nanostructures of $NiMoO_4$-based composite materials for supercapacitor applications. Such nanostructures using various $NiMoO_4$ composites are elaborated in detail with highlights on how the selected material and the corresponding morphology affect the electrochemical features of supercapacitors. Finally, the pre-existing challenges to this approach are addressed with a discussion on how to improve the overall performance of supercapacitors based on $NiMoO_4$-based core-shell nanostructured composites.

2. Properties of NiMoO$_4$

2.1. Crystal Structure

At atmospheric pressure, $NiMoO_4$ exists in 2 phases, namely, a low-temperature α-phase and a high-temperature β-phase. Both phases belong to the monoclinic crystal structure, as shown in Figure 2. The crystal symmetry consists of space group *C2/m*. The lattice parameters are a = 9.582 Å, b = 8.763 Å, and c = 7.619 Å [20]. A major difference between the 2 phases is in the anisotropic coordination of the Mo^{6+} ions. The α- and β-phases of $NiMoO_4$ are obtained when the Mo^{6+} ions occupy octahedral sites (MoO_6) and tetrahedral sites (MoO_4), respectively. But Ni^{2+} ions occupy only octahedral sites in both phases [21–23]. Interestingly, the edge-sharing NiO_6 octahedral sites are interconnected by MoO_4 tetrahedral sites to establish a 3D network structure with open channels, which is advantageous for ion diffusion [20]. Further, the α-phase presents doubly ionized vacancies, while the β-phase presents singly ionized vacancies. The α→β phase transition commonly takes place at a temperature of around 600 °C. Hence, the temperature is the main factor in determining the phase and the degree of crystallinity of $NiMoO_4$. Indeed, when compared to good crystallinity, poor crystallinity is recommended for excellent

supercapacitive behavior because it leads to more pathways for electrolyte infiltration and ion transport [24].
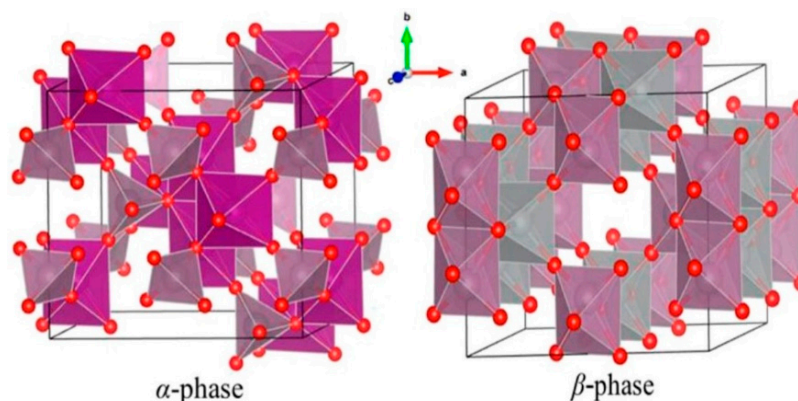

Figure 2. The monoclinic crystal structures of α-NiMoO$_4$ and β-NiMoO$_4$ [21]. Reproduced from Ref. [21] with permission from AIP Publishing, 2018.

2.2. Electrical Conductivity

Generally, in NiMoO$_4$, the Mo^{6+} atom contributes to the intrinsic electrical conductivity, whereas not involved in the redox reaction [25]. The conductivity is of the order of 10^{-6} Scm^{-1}, and notably, β-NiMoO$_4$ has higher conductivity than α-NiMoO$_4$ [26,27]. Indeed, the conductivity of NiMoO$_4$ depends on the band gap energy (E$_g$~2.81 eV) and compared to carbon materials, is usually unsatisfactory. Fortunately, the process of compositing, doping, and introducing oxygen vacancies could improve the conductivity of NiMoO$_4$. In addition, the nature of the substrate has a significant influence on the conductivity. If the synthesized material is in a powder form, a binder and conductive reagent are used in the electrode fabrication. The additives can increase the internal resistance and dead volume with an inefficient use of active material, which is unfavorable for electron/ion transfer during the redox reaction, leading to low specific capacitance and poor rate capability. To solve this problem, binder-free NiMoO$_4$ electrodes can be prepared by directly growing the material on conductive substrates like Ni foam (NF), Ti foil, carbon cloth (CC), and graphite paper [20,28]. These substrates act as the current collector, and their intrinsic advantages include a high specific surface area (SSA), a macroporous structure, and superior electrical conductivity.

2.3. Morphology

The supercapacitive performance is closely associated with the material structure. Since NiMoO$_4$ is a pseudocapacitive material, its SSA matters for redox reactions that occur at the electrode surface. A larger SSA indicates the presence of a larger number of electroactive sites for the redox process. The SSA of metal oxides mostly depends on the nanostructure. The construction of a nanostructure with unique pore size and large SSA would enhance the capacitance of electrode material. With the aim of developing supercapacitor electrodes of high performance, NiMoO$_4$ nanostructures with various morphologies have been attempted, such as nanowires [29], nanospheres [30], nanorods [31], nanosheets [20], nanoflowers [32], and nanoflakes [33]. For example, Cai et al. [34] described NiMoO$_4$ nanorods and nanospheres as α- and β- phases, respectively. NiMoO$_4$ nanospheres assembled from thin mesoporous nanosheets showed high specific capacitance, good rate capability, and cycling stability, which were attributed to a high surface area (58.2 m^{2}g^{-1}, pore volume is 0.218 cm^{3}g^{-1}) and high electrical conductivity when compared to NiMoO$_4$ nanorods (13.5 m^{2}g^{-1}, pore volume is 0.030 cm^{3}g^{-1}). At a current density of 1 Ag^{-1}, the specific capacitance was 974.4 Fg^{-1} with a remarkable energy-density of 20.1 Whkg^{-1} and a power-density of 2100 Wkg^{-1}.

NiMoO$_4$ nanosheets are superior to NiMoO$_4$ nanorods in terms of both specific capacitance and cycling stability. The high porosity of nanosheets ensures a high SSA (surface

area~79 m^2g^{-1} and pore size < 10 nm) that is much larger than that of nanorods (surface area~41 m^2g^{-1}). This relatively enlarges the electrode/electrolyte contact area and offers abundant active sites for a rapid redox reaction, resulting in improved specific capacitance. Moreover, nanosheets are much thinner than nanorods, supporting fast electron/ion transport, whereas they are likely to resist volume change during the charge/discharge cycles [20].

3. Synthesis

Synthesis methods have a significant impact on the morphology, crystallite size, conductivity, and electrochemical performance of electrode materials. A variety of methods are employed for synthesizing $NiMoO_4$, such as hydrothermal, microwave-assisted synthesis, electrodeposition, etc. Some common methods are briefly discussed in this section.

3.1. Hydrothermal Method

The hydrothermal method commonly used for efficiently preparing metal oxide nanostructures requires no complex, sophisticated equipment. In this method, the precursors are dissolved in deionized water, and the pH value is regulated by adding acid or base into the precursor solution. The solution is then transferred into a Teflon-lined stainless steel autoclave to complete the reaction at a temperature over 100 °C for a specific duration of time. The end-product is centrifuged, collected, and finally dried in a vacuum. Compared to other chemical techniques, this method can produce nanostructures of high purity with various types of morphology [35–37].

Cai et al. [38] produced ultrathin mesoporous $NiMoO_4$ nanosheets using a one-step hydrothermal method. Even at a high current density of 20 Ag^{-1}, the material still maintained a specific capacitance of up to 1200.5 Fg^{-1} and capacitance retention of about 75% as the charge/discharge rate changes from 2 to 20 Ag^{-1}. The superior electrochemical performance was attributed to ultrathin mesoporous structure and high electrical conductivity. The hydrothermal method also offered the robust advantage of preparing binder-free nanostructures directly on NF-like conductive substrates. Adhesion between the nanostructured network and NF allowed for fast electron transport, efficiently enhancing the cycling stability and rate capability even at high current density. The 3D $NiMoO_4$ nanoplate arrays synthesized on NF produced a capacitance of 3.4 Fcm^{-2} at 2 $mAcm^{-2}$ with notable cycling stability (87% capacity retention after 3000 cycles) [39]. Hong et al. [40] also reported, by a hydrothermal method, the solubility-dependent $NiMoO_4$ nanostructures, with a capacitance of 1335 Fg^{-1} at 1 Ag^{-1} and cycling stability of 81.3% over 3000 charge/discharge cycles. Feng et al. [41] synthesized $NiMoO_4$ nanoflakes on an N-doped graphene surface, which displayed a specific capacitance of 1913 Fg^{-1} at 1 Ag^{-1}.

3.2. Microwave-Assisted Method

The microwave-assisted synthesis offers certain advantages over hydrothermal methods, such as cleanliness, high efficiency, low energy consumption, nucleation, and crystallization in a short time duration [42]. The sheet-like $NiO/NiMoO_4$ hybrid nanostructures synthesized by this method exhibited a higher specific capacitance (1147.5 Fg^{-1}) at 1 Ag^{-1} compared to the material synthesized using the hydrothermal approach (677.8 Fg^{-1}). In another work, the 2D amorphous $NiMoO_4$ nanoflakes prepared by this technique showed a high specific capacitance of 1650 Fg^{-1} [43].

3.3. Electrodeposition Method

The electrodeposition method is also used to develop $NiMoO_4$ nanostructures in a three-electrode system. The end products are deposited on the conductive substrate in a homogeneous solution comprising the precursor salts. Typically, the method is employed by a subsequent thermal annealing process to prepare a nanoporous structure. For example, Kumbhar et al. [44] synthesized a honeycomb-like $NiMoO_4$ structure with a range of electrochemical cycles (40, 60, 80, and 100). The electrode obtained by 80 cycles exhibited

a high specific capacitance of 1475 Fg^{-1} at 1 Ag^{-1} and a good rate capability of 72.8% at 20 Ag^{-1}, while the electrode exhibited 87.9% capacitive retention after 5000 cycles.

4. Composites of NiMoO$_4$ Core-Shell Nanostructures for Use as Electrode Materials

A core-shell structure usually consists of a sphere-shaped central medium, i.e., a core, with a concentric film around it, i.e., a shell. This structure can be configured by joining two materials with different inherent properties, for instance, a core with high electrochemical activity and a shell with high electrical conductivity. The synergistic effect of the use of heterogeneous materials for a core and a shell can lead the supercapacitor of the core-shell format to possess better energy storage ability compared to a single material-based structure.

The core material efficiently transfers the charges while contributing to electro-capacitance. As the core materials, carbon materials, metals, metal chalcogenides, and metal oxides have been used. Among those, carbon materials and metals are known to benefit from high conductivity that ensures efficient charge transfer during the charge/discharge process. Meanwhile, the shell, i.e., a thin layer that is grown on the core and would thus exhibit similar morphological properties to the core, has the role of affording a high surface area for accumulating charges and providing a huge number of active sites to conduct redox reactions. Carbon materials, conductive polymers, semiconductors, metal sulfides, and metal oxides could be used as shell materials [45,46].

NiMoO$_4$, a naturally abundant pseudocapacitive metal oxide, has been considered a good candidate for either a core or shell material due to its natural abundance, the material's low cost, exceptional redox reaction, and wide electrochemical potential window in cyclic voltammetry. Nevertheless, the primary concern regarding the use of the NiMoO$_4$ nanoparticles would arise from the material-intrinsic low electrical conductivity and the high probability of aggregation of the particles. This could limit electron/ion transport, thus reducing overall electrochemical performance [47,48]. To tackle the challenges, the rational design of a hybrid core-shell nanostructured electrode of NiMoO$_4$-based composite materials can be an alternative to boost overall electrochemical characteristics, including rapid electron/ion transfer kinetics, high specific capacitance, and fine structural tunability. The NiMoO$_4$-based composite materials consist of NiMoO$_4$ with metal oxides (ZnCo$_2$O$_4$, SnO$_2$)/metal hydroxides (NiCo-LDH)/metal chalcogenides (NiCo$_2$S$_4$, Ni$_3$S$_2$)/carbon materials (CNTs, graphene, activated carbons, etc.)/conductive polymers (PANI, PPy).

4.1. NiMoO$_4$-Metal Oxide Composite

The NiMoO$_4$-metal oxide composite has been used for core-shell nanostructured electrodes due to good electrochemical features [49–51]. Table 1 summarizes the electrochemical properties of the core-shell nanostructures of this kind of composite reported in the literature. MnO$_2$, a metal oxide with pseudocapacitive properties, has been incorporated into NiMoO4 nanowires, forming the hybrid core-shell structure, i.e., NiMoO$_4$-MnO$_2$ on CC [52]. During the hydrothermal synthesis, the NiMoO$_4$ nanowire acted as a 'backbone' to guide the MnO$_2$ self-assembling growth in an aqueous solution without surfactant and stabilizer, as shown in Figure 3a. Figure 3b illustrates that NiMoO$_4$ nanowires were tightly attached to MnO$_2$ nanoflakes. The presence of spacing between NiMoO$_4$ nanowires facilitated electrolyte ion diffusion into the inner region of electrodes, and the CC could offer abundant electron transfer channels to enhance the electrochemical performance (Figure 3c). The hybrid nanostructure of NiMoO$_4$-MnO$_2$ delivered a higher areal capacitance (3.90 Fcm^{-2} at 8 mAcm^{-2}) than NiMoO$_4$ nanowires. NiMoO$_4$-MnO$_2$ nanosheet arrays on Ti mesh showed a specific capacitance of 976 Fg^{-1} at 1 Ag^{-1} [53]. The 3D α-NiMoO$_4$-δ-MnO$_2$/NF nanorod/nanosheet structures were fabricated through hydrothermal and chelation-mediated aqueous processes [54]. The specific capacitance initially decreased at cycles up to 1000 due to the increase of equivalent series resistance. After 1000 cycles, the petal-like δ-MnO$_2$ nanosheets served as a protective layer to keep the grass-like α-NiMoO$_4$ structural integrity during the remaining redox reaction. As a result,

superior cycling life with a 101.9% capacitance retention rate was attained (5000 cycles), being much better than that of α-NiMoO$_4$ nanorods (78.5%). The 1D MnO$_2$-NiMoO$_4$ nanostructured electrode delivered a maximum specific capacitance of 1123.7 Fg^{-1} at a scan rate of 5 mVs^{-1} and a super-long cycling life with a 115.5% retention rate after 5000 cycles [55]. It also possessed tremendous flexibility, without obvious change of specific capacitance after bending (30°–150°).
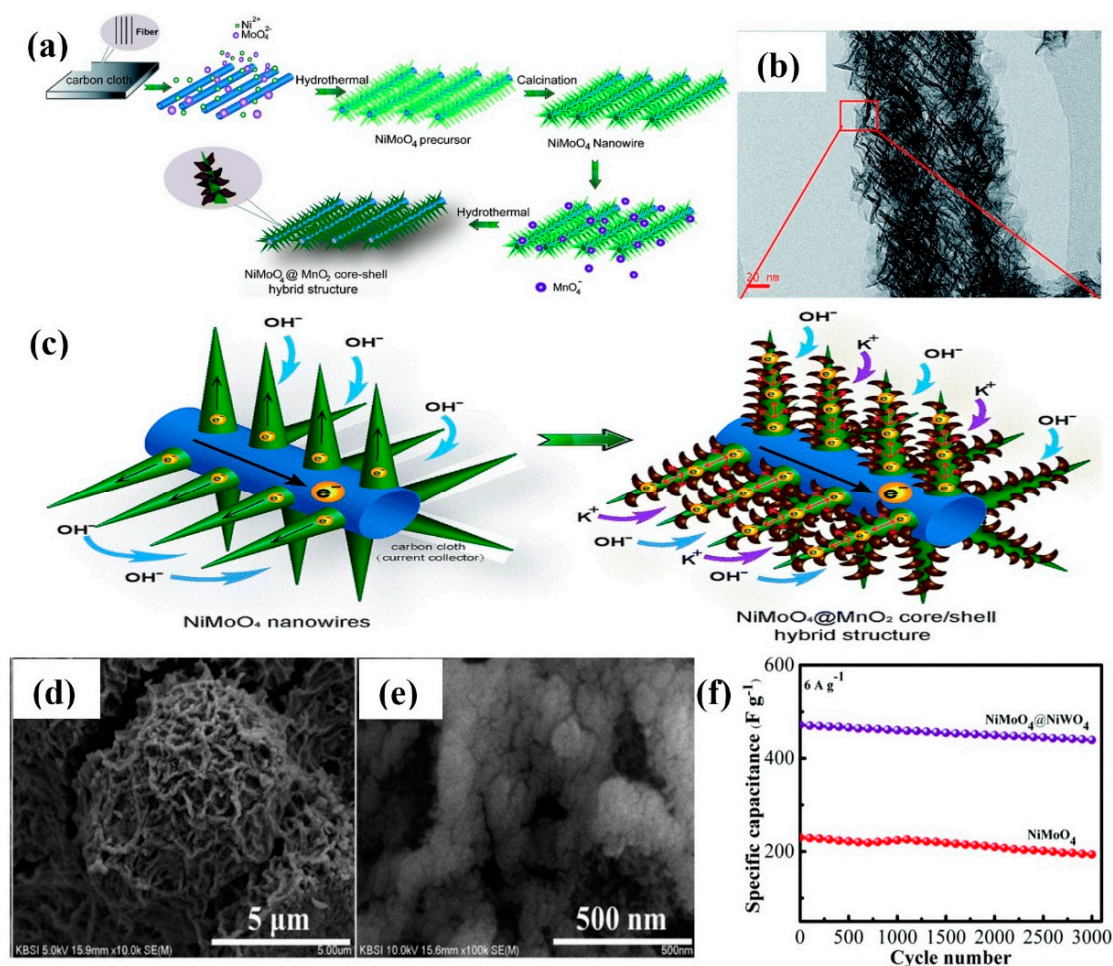

Figure 3. (**a**) Schematic diagram of the fabrication process of NiMoO$_4$−MnO$_2$ core−shell hybrid structure, (**b**) TEM image of NiMoO$_4$−MnO$_2$ scratched from CC, (**c**) Schematic diagram showing the charge storage advantage of NiMoO$_4$−MnO$_2$ [52]. Reproduced from Ref. [52] with permission from The Royal Society of Chemistry, 2015. (**d**,**e**) SEM images of NiMoO$_4$−NiWO$_4$ electrode on NF at different magnifications, (**f**) Cyclic performance of NiMoO$_4$ and NiMoO$_4$−NiWO$_4$ electrodes [56]. Reproduced from Ref. [56] with permission from The Royal Society of Chemistry, 2018.

Co$_3$O$_4$ has received special attention because of its superior capacitance (3560 Fg^{-1}), easy synthesis, good electrochemical stability, and great reversibility [57]. Therefore, the NiMoO$_4$-Co$_3$O$_4$ composite was anchored on rGO/NF for different reaction times (1, 3, 5, and 7 h) [58]. With increasing the scan rate (5–50 mVs^{-1}), the CV plots of the NiMoO$_4$-Co$_3$O$_4$-5H electrode maintained a similar form. Besides, the shift of cathodic and anodic peaks toward negative and positive potentials was ascribed to the resistance and polarization effect of the electrode, respectively. At a low scan rate, the rate of ion diffusion was greater than that of the electron release. At a high scan rate, the redox peak shift was due to the limited intercalation of electrolyte ions into the dense center of the composite, while ion diffusion was inadequate to satisfy electron neutralization. The composite combined the advantages of the large specific capacitance of NiMoO$_4$ and the great rate

capability of Co_3O_4. The prepared $NiMoO_4$-Co_3O_4-5H composite exhibited a specific capacitance of 1722.3 Fg^{-1} at 1 Ag^{-1}, a good rate capability of 80.8% at 10 Ag^{-1} and cycling stability of 91.1% (6000 cycles). High Coulombic efficiency of about 99.4% showed good electrochemical reversibility.

Many research groups employed hydrothermal methods to grow the $NiMoO_4$ nanosheets on the backbone of Co_3O_4 material and prepare the hierarchical 3D Co_3O_4-$NiMoO_4$ heterostructure on NF and CC [59–64]. Hierarchical Co_3O_4-$NiMoO_4$ core-shell nanostructure may hold the advantages of improved rate capability resulting from Co_3O_4 nanowires and high SSA of $NiMoO_4$ nanosheets. Hu and co-workers [65] utilized MOF-derived Co_3O_4 nanosheets and $NiMoO_4$ nanosheets as core and shell materials, respectively. ZIF-67 precursor was converted into leaf-like Co_3O_4 through calcination in air. The areal-specific capacitance achieved a maximum of 2.3 Fcm^{-2} at 1 $mAcm^{-2}$ due to the high mass loading and the synergistic effect of materials. Dong et al. [66], for the first time, synthesized tube-like Co_3O_4-$NiMoO_4$ yolk-shell composite via a two-step hydrothermal route. Here, ultrathin $NiMoO_4$ nanosheets (thickness~200 nm) are vertically arranged and interconnected together to develop a porous shell, covering the Co_3O_4 fiber with interspaces between the core and shell. The unique mesoporous structure enhances the contact area of the electrode and electrolyte, as well as increases the electrochemically active sites. All CV curves tested under different scan rates (5–100 mVs^{-1}) show a pair of strong redox peaks, representing the pseudocapacitive behavior. The specific capacitance reached 998.05 Fg^{-1} at 0.5 Ag^{-1}. Ultrathin and porous $NiMoO_4$-$CoMoO_4$ nanoflakes were constructed on hollow Co_3O_4 nanowires through a hydrothermal route, followed by an activation process in the presence of KOH and calcination treatment at 700 °C [67]. The role of KOH (excessive and without) on the porous structure of Co_3O_4-$NiMoO_4$-$CoMoO_4$ heterostructure was analyzed. After the KOH activation, both the pore volume and SSA (253.5 m^2g^{-1}) increase. This is due to the Co-precursor decomposition and reaction with KOH at 700 °C, creating K_2CO_3, H_2O, and CO_2, which makes tiny holes in the end- product. The long-range ordered 3D porous structure produces nanopores of~2–5 nm in size. But the excess KOH induces aggregation and strong gas formation, resulting in the bulk composite. The high SSA, improved mass transfer, open and porous nanostructure, and more active sites contributed to electrochemical performance. The enhanced use of $NiMoO_4$-$CoMoO_4$ shell layer on the Co_3O_4 core helps to gain extra electrons, which increases the OH^- adsorption at the shell surface, leading to high specific capacity (272 $mAhg^{-1}$ at 1 Ag^{-1}). This work paved the way to synthesize materials with the structure of M_3O_4-$MMoO_4$-$MMoO_4$ (M = Fe, Ni, Sn, etc.).

The binary metal oxides usually display better electrochemical performance than the single metal oxides. Particularly, the transition metal cobaltites, such as $NiCo_2O_4$, $ZnCo_2O_4$, $CuCo_2O_4$, and $MnCo_2O_4$, have multiple oxidation states as well as high electrical conductivity. $NiCo_2O_4$ is popular because of its fast reversible redox reactions, therefore integrated with $NiMoO_4$ to increase the specific capacitance and rate capability [68–71]. Hierarchical $NiCo_2O_4$-$NiMoO_4$/NF nanowire/nanosheet arrays (NWSAs) were synthesized by changing hydrothermal reaction time (4, 8, 12, and 16 h) [72]. In Figure 4a, the TEM image reveals that the $NiCo_2O_4$ nanowire is covered by a $NiMoO_4$ nanosheet. Even for a long reaction time (12 h), the shell region of the interconnected network consisting of highly porous $NiMoO_4$ nanosheets is retained well, which can offer more electroactive sites for redox reactions. HRTEM measurements of the shell material exhibit a set of clear lattice fringes with an interplanar spacing of ca. 0.214 nm, corresponding to the (121) planes of $NiMoO_4$ nanosheets (Figure 4b,c). The EDS mapping images confirm that the $NiMoO_4$ shell material is effectively coated on the backbone of the $NiCo_2O_4$ nanowire, as displayed in Figure 4d. The development of a 3D interconnected network is advantageous for facile electrolyte infiltration and rapid electron transport. All the CV curves show a similar shape even at a high scan rate of 50 mVs^{-1}, indicating outstanding electrochemical reversibility and high-rate performance (Figure 4e). Figure 4f represents the discharge curves of the $NiCo_2O_4$-$NiMoO_4$ electrode (12 h) with a potential range of 0–0.5 V at differ-

ent current densities (10–80 mAcm^{-2}). The optimized $NiCo_2O_4$-$NiMoO_4$ electrode (12 h) delivered a good areal capacitance of 5.80 Fcm^{-2} at 10 mAcm^{-2} (Figure 4g). The asymmetric supercapacitor (ASC) of $NiCo_2O_4$-$NiMoO_4$//AC attained a high energy-density of 21.7 Whkg^{-1} (Figure 4h,i). Both reaction time and growth temperature strongly influence the morphology of $NiCo_2O_4$-$NiMoO_4$/NF nanowires [73]. For an 8 h reaction time, the $NiCo_2O_4$ core surface was almost covered by small $NiMoO_4$ nanoflakes. At a low temperature of 80 °C, the rod-like morphology was obtained. When the temperature increased to 120 °C, nanorods were broken and perfectly formed as nanowire arrays at 160 °C. However, at 200 °C, nanowires fully disappeared and mostly grew into nanosheets. At 240 °C, these nanosheets were completely interconnected with each another, creating an intricate transportation network. The areal and mass-specific capacitances were 7.55 Fcm^{-2} and 1242 Fg^{-1}, respectively, at 10 mAcm^{-2}. By changing the reaction time, nanosheets and nanoplates of $NiMoO_4$ were grown onto the backbone of $NiCo_2O_4$ (nanowires and nanosheets), and the electrode performance was considerably good [74–76]. For $NiMoO_4$, it is clear that the sheet-like morphology can be observed at a prolonged reaction time.
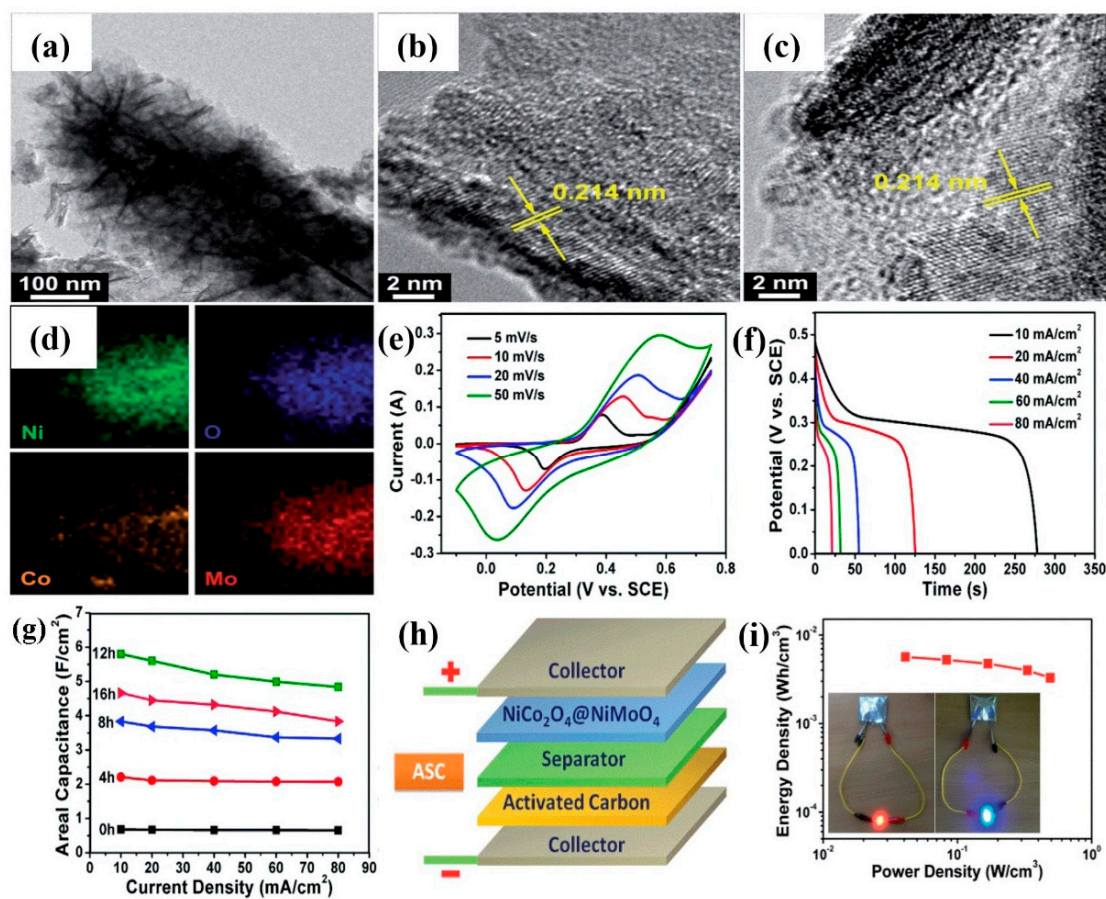
Figure 4. (**a**) TEM image of $NiCo_2O_4-NiMoO_4$ (4 h) core−shell hybrid nanostructure, (**b,c**) HRTEM images corresponding to the shell region, (**d**) EDS mapping images, (**e**) CV curves of $NiCo_2O_4-NiMoO_4$ NWSAs (12 h) at different scan rates, (**f**) Discharge curves of $NiCo_2O_4-NiMoO_4$ NWSAs (12 h) at various current densities, (**g**) Areal capacitance of the electrode with respect to current density, (**h**) Schematic illustration of the assembled ASC device, (**i**) Ragone plot of the device, inset shows the red and blue LEDs lit up by two assembled ASC devices joined in series [72]. Reproduced from Ref. [72] with permission from The Royal Society of Chemistry, 2015.

A flexible and binder-free electrode of $NiCo_2O_4$-$NiMoO_4$ nanowires was grown on CC [77]. Because of the high electrical conductivity of $NiCo_2O_4$, electrons can easily transport between CC and $NiMoO_4$ nanosheets via the backbone of $NiCo_2O_4$ nanowires. The

areal capacitance was 2.917 Fcm^{-2} at 2 mAcm^{-2}, and cycling stability was 90.6% (after 2000 cycles). Hong and co-workers [78] constructed NiCo$_2$O$_4$ and NiCo$_2$O$_4$-NiMoO$_4$ nanostructures on two different substrates (NF and CC). They investigated the effect of substrate on morphology, surface area, and porous structure. Interestingly, the morphology was nearly independent of the substrate. A large surface area and pore volume were attained for the electrode corresponding to CC. However, NiCo$_2$O$_4$-NiMoO$_4$/NF showed better performance due to the high electrical conductivity and the formation of the nickel oxide/hydroxide layer on NF. NiMoO$_4$ nanosheet arrays were grown on sea urchin-like NiCo$_2$O$_4$ to develop a mesoporous 3D NiCo$_2$O$_4$-NiMoO$_4$ structure [79]. The 3D honeycomb-like structure of NiCo$_2$O$_4$-NiMoO$_4$ nanofilm/nanoflake arrays was synthesized on NF [80]. Hierarchical NiCo$_2$O$_4$-NiMoO$_4$ nanostructures were designed with two different morphologies of NiCo$_2$O$_4$ scaffolds (uninterrupted nanosheet arrays (UNSAs) and nanoneedle arrays (NNAs)), and the effect of morphology on the electrochemical performance was investigated [81]. At 2 mAcm^{-2}, the NiCo$_2$O$_4$-UNSA-NiMoO$_4$ electrode delivered a high areal-specific capacitance and mass-specific capacitance of 7.29 Fcm^{-2} and 1941 Fg^{-1}, respectively. But the corresponding values for NiCo$_2$O$_4$-NNA-NiMoO$_4$ were 5.96 Fcm^{-2} and 1560 Fg^{-1}. Further, the NiCo$_2$O$_4$-UNSA-NiMoO$_4$ electrode showed outstanding rate capability (84.1%) at 60 mAcm^{-2}, compared to NNA-NiMoO$_4$ (73.5%). This electrochemical superiority is largely assigned to ultrathin NiMoO$_4$ nanosheets and hierarchical mesoporous structure, due to which the electroactive surface area increased; therefore, ion transport became easier within the electrode. Moreover, the UNSAs electrode can produce enhanced reversibility and lower charge transfer resistance (0.758 Ω) compared to NNAs (1.438 Ω), particularly at long charge/discharge cycles. Due to the larger lateral size of ~2–4 μm and interconnection, NiCo$_2$O$_4$ nanosheets provided more electron transport channels, resulting in low resistance. But, in the case of NiCo$_2$O$_4$ nanoneedles, the electrical conductivity was very much limited by its cusp feature.

The multi-dimensional NiCo$_2$O$_4$-NiMoO$_4$ nanowire/nanosheet arrays were hydrothermally synthesized on CC [82]. The shell thickness of NiMoO$_4$ was controlled by urea. The thick NiMoO$_4$ shell serves as a protective layer to forbid the structural collapse of NiCo$_2$O$_4$ nanowires during the redox reaction. Due to the high SSA, large pore volume, low charge transfer resistance, and improved strain accommodation, the NiCo$_2$O$_4$-NiMoO$_4$ electrode with a thick NiMoO$_4$ shell exhibited favorable electrochemical performance, delivering a high areal capacitance of 2522 mFcm^{-2} at 1 mAcm^{-2}. Even after 5000 cycles, the core-shell structure was sustained, and NiCo$_2$O$_4$ nanowires remained largely unaffected without structural collapse. Hong et al. [83] reported that substrate has a great influence on the morphology of NiCo$_2$O$_4$-NiMoO$_4$ rather than a structure-directing agent (SDA). They used different structure-directing agents (urea, hexamethylenetetramine (HMT), and ammonium fluoride (NH$_4$F)) and substrates (NF and CC). When NF was used, the electrochemical performance was better. The highest specific capacitance (C$_F$) of 4.05 Fcm^{-2} was obtained for the NiCo$_2$O$_4$-NiMoO$_4$/NF electrode synthesized by NH$_4$F, which is assigned to the smallest R$_s$ (1.24 Ω) and R$_{ct}$ (0.99 Ω) values arising from the influence of NF substrate, even if the surface area of active material is too small (14.52 m^{2}g^{-1}). The assembled device delivered excellent Coulombic efficiency (more than 95%), as well as flexibility without any capacitance decay under 150° bending. The highly ordered and vertically aligned NiCo$_2$O$_4$ nanoflakes covered by NiMoO$_4$ nanoparticles were synthesized by electrochemical deposition [84]. The NiCo$_2$O$_4$/NiMoO$_4$ electrode exhibited enhanced performance with a specific capacitance of 3705 Fg^{-1} at 1.5 Ag^{-1} and a rate capability of 3525 Fg^{-1} at 30 Ag^{-1} (95.1%). The cycling stability was assessed for the first 5000 charge/discharge cycles at 30 Ag^{-1}. With the increasing number of cycles, the specific capacitance slightly improved and attained its maximum at 3530 Fg^{-1}. This was explained by the electromotive force created due to the applied current density so that electrolyte ions enter into the pores of the active material. As a result, the heterogeneous surface transit from the Cassie-Baxter state to the Wenzel state. After 5000 cycles, 94.6% of initial capacitance was retained. This may be due to the electrochemically and/or mechanically detached active material arising

from the strain produced during the Faradaic redox reactions. The 3D flower-like $NiCo_2O_4$-$NiMoO_4$/rGO hybrid composite was grown on NF [85]. Urchin-like $NiCo_2O_4$ nanoneedles were covered by crosslinked $NiMoO_4$ nanoflakes, over which rGO nanosheets were deposited. The $NiMoO_4$ nanoflakes spatially filled the $NiCo_2O_4$ nanoneedle surface and gaps between them, producing a porous structure together with high SSA (~79.7 m^2g^{-1}, pore volume~0.24 cm^3g^{-1}); meanwhile, rGO contributed to improved electrical conductivity. Therefore, a high areal specific capacitance of 9.41 Fcm^{-2} (1837.89 Fg^{-1}) at 10mAcm^{-2} was achieved, along with 75% capacitance retention after 2000 cycles. After the cycle test, the overall 3D porous structure and morphology were still preserved. Nevertheless, the GO coating realized some damage due to multiple cycles. The honeycomb structure of the $NiMoO_4$-$NiCo_2O_4$/NF electrode with folded and silk-like morphology was fabricated using chemical bath deposition [86]. It exhibited a high specific capacitance of 2695 Fg^{-1} at 20 mAg^{-2}, which was better compared to $NiCo_2O_4$ nanoplates (1018 Fg^{-1}) and $NiMoO_4$ honeycombs (1194 Fg^{-1}).

Recently, attention has been paid to $ZnCo_2O_4$ owing to its high theoretical capacitance, rich redox reaction, and diverse morphology [87]. A smart strategy was used to construct a reduced-$ZnCo_2O_4$-$NiMoO_4\cdot H_2O$ core-shell heterostructure [88]. $ZnCo_2O_4$ and $NiMoO_4\cdot H_2O$ were hydrothermally synthesized, and oxygen vacancies were introduced into $ZnCo_2O_4$ through chemical reduction (r$ZnCo_2O_4$), which led to the wrinkled surface of $ZnCo_2O_4$ nanowires, along with poor crystallinity. The excess oxygen vacancies destroyed the integral structure, which resulted in poor electrochemical performance. The optimized electrode of r$ZnCo_2O_4$-$NiMoO_4\cdot H_2O$ (for 3 h) showed the highest areal capacitance of 3.53 Fcm^{-2}, which was higher than that of r$ZnCo_2O_4$ (3 h) (127.7%) and the pristine $ZnCo_2O_4$ (320.2%). The improved cycling stability is due to the large electrical conductivity and abundant active sites introduced by oxygen vacancies. In the case of 3D $ZnCo_2O_4$-$NiMoO_4$ heterostructure developed on NF, the plate-like $ZnCo_2O_4$ was confirmed to be covered by interconnected $NiMoO_4$ nanosheets [89]. The surface of $ZnCo_2O_4$ plates consists of highly-entangled grains and pore channels (pore size~10–20 nm). HRTEM images and the fast Fourier transform diffraction (FFT) patterns revealed two distinct regions in the $ZnCo_2O_4$/$NiMoO_4$ heterostructures: the primary region consists of $NiMoO_4$ shell and rigid $ZnCo_2O_4$ core, and the secondary region linked with the layered $NiMoO_4$ nanosheets. The stable, porous, and conductive features benefitted the high areal and mass-specific capacitances of 6.07 Fcm^{-2} and 1480.48 Fg^{-1}, respectively, at 2 $mAcm^{-2}$. $NiMoO_4$ nanosheet arrays were hydrothermally grown on $ZnCo_2O_4$ nanowires anchored on NF. At 1 Ag^{-1}, the specific capacitance reached a maximum of 1912 Fg^{-1} [90]. In another work, different nanostructures of $ZnCo_2O_4$ (nanowires and nanosheets) were used as skeletons to grow $NiMoO_4$ [91]. The $ZnCo_2O_4$-$NiMoO_4$ nanosheets delivered high specific capacity (1158 Cg^{-1} at 10 $mAcm^{-2}$) and excellent cycling stability (103.4% after 5000 cycles), which was much better than that of $ZnCo_2O_4$-$NiMoO_4$ nanowires (913.5 Cg^{-1}). The reason might be the unique nanostructure, where the $ZnCo_2O_4$ nanosheets are strongly interconnected to maximize the surface exposure and also shorten the ion transport distance. Additionally, the $NiMoO_4$ shell layer provided structural integrity and low IR drop during the charge/discharge process.

In $CuCo_2O_4$-$NiMoO_4$/NF nanowire-nanosheet arrays (diameter~300 nm), $NiMoO_4$ nanosheets were closely covered on $CuCo_2O_4$ nanowires, and shell thickness was~100 nm [92]. A pair of strong redox peaks is due to the reversible processes of Ni^{3+}/Ni^{2+}, Cu^{2+}/Cu^+, and Co^{4+}/Co^{3+}. The specific capacitance reached 2207 Fg^{-1} at 1.25 Ag^{-1}, and the capacitance loss was only about 4.4% from its initial value after 5000 cycles. Urchin-like $CuCo_2O_4$-$NiMoO_4$ architecture was constructed on NF [93]. The $CuCo_2O_4$ microspheres consist of 1D $CuCo_2O_4$ nanoneedles oriented and assembled in a radial form from the center to offer open space, enhancing the charge transport. For a 4 h reaction time, a maximum specific capacity of 276 $mAhg^{-1}$ was achieved at 1 Ag^{-1}. This is ascribed to the 2D $NiMoO_4$ nanosheets, which can increase the active sites, ease ion transport, and diminish the volume change during long-term cycling. The $MnCo_2O_4$-$NiMoO_4$/NF electrode exhibited an improved

specific capacitance of 1244 Fg^{-1} at 1 Ag^{-1} and a rate capability of 91% at 10 Ag^{-1} [94]. The $MnCo_2O_4$ nanowire acted as a template for the homogeneous nucleation of the outer $NiMoO_4$ nanosheet shell. The average pore size was 8.5 nm, which benefitted the ion diffusion inside the electrode material. The $MnCo_2O_4$-$NiMoO_4$ nanoneedles/nanoflakes achieved a specific capacitance of up to 1718 Fg^{-1} at 1 Ag^{-1} [95]. Double urchin-like $MgCo_2O_4$-$NiMoO_4$/NF displayed good physical and chemical structures, as well as excellent electrochemical properties [96]. At 1 Ag^{-1}, the optimized electrode (12 h reaction time) produced a specific capacitance of 1775 Fg^{-1}. In another work, $CoMoO_4$ and $NiMoO_4$ shell materials were separately loaded on $MgCo_2O_4$ nanosheet arrays supported on NF [97]. The specific capacity of $MgCo_2O_4$-$NiMoO_4$ (1111.57 Cg^{-1} at 1 $mAcm^{-2}$) was higher than that of $MgCo_2O_4$-$CoMoO_4$ (1089.94 Cg^{-1}).

Venus flytrap-like NiCoMn-O-$NiMoO_4$-C nanosheet arrays supported on CC substrate were developed for different reaction temperatures (80, 100, and 120 °C) and reaction times (2, 4, and 6 h) [98]. The NiCoMn-O-$NiMoO_4$ core nanosheet arrays (thickness~256 nm) with self-decorated nanoneedles act as the conductive backbone because of their trimetallic nature. The NiCoMn-O created extra electrochemically active sites for electrolyte permeation, and the $NiMoO_4$ layer contributed to the high electrochemical activity. The carbon shell layer (thickness~4 nm) improved the rate capability by shortening the electron transport path and increasing the cycling stability by reducing the volume swelling during the redox process. Therefore, a high specific capacitance value of 2189.5 Fg^{-1} (at 0.25 Ag^{-1}) was attained. The 3D porous ZnNiCo-O-$NiMoO_4$ nanowire/nanosheet arrays (NWNSAs) were prepared on NF by an additive-free hydrothermal process [99]. Because of the uniform distribution of mesopores (average pore diameter~3.8 nm) all over the surface of the polycrystalline $NiMoO_4$ nanosheets, ZnNiCo-O-$NiMoO_4$ NWNSAs offered excellent conductivity, durability, and appropriate channels for the fast transfer of electrons/ions. At 3 $mAcm^{-2}$, a higher specific capacity (338.5 $mAhg^{-1}$) was achieved compared to the ZnNiCo-O electrode (266.1 $mAhg^{-1}$). After 10,000 cycles, the capacity retention was 86%. The ASC assembled with Fe_2O_3/graphene hydrogel anode showed an excellent specific capacity of 87.5 $mAhg^{-1}$ at 4 $mAcm^{-2}$.

$CoMoO_4$-$NiMoO_4 \cdot xH_2O$ heterostructure was hydrothermally prepared on carbon fabric (CF) [100]. With increasing reaction time (1–10 h), $NiMoO_4$ nanosheets were largely covered over $CoMoO_4$ nanowires. Scanning electron microscopy (SEM) images revealed that $NiMoO_4 \cdot xH_2O$ nanosheets are uniformly covered on the $CoMoO_4$ nanowire surface, creating an interconnected and highly porous structure that will provide a network structure for fast electron transportation, abundant active sites for ion diffusion, and good strain accommodation. Under different scan rates (5–100 mVs^{-1}), each CV curve shows a pair of redox peaks, representing the pseudocapacitive behavior. The specific capacitance is mostly linked with the quasi-reversible electron-transfer kinetics originating from Ni^{2+}/Ni^{3+} and Co^{2+}/Co^{3+} redox reactions and possibly mediated by OH^- ions in the electrolyte. The Mo ion is not included in redox reactions but contributes to electrical conductivity. Consequently, the $CoMoO_4$-$NiMoO_4 \cdot xH_2O$ electrode yielded a maximum specific capacitance of 1582 Fg^{-1} at 1 Ag^{-1}. Also, nanobundles of $CoMoO_4$-$NiMoO_4.xH_2O$ were synthesized by chemical coprecipitation using $CoMoO_4$ nanorods as backbone material [101]. The effect of the Ni-Co mass ratio and reaction time on the electrochemical properties was investigated. The specific capacitance improved with increasing Ni-Co mass ratio and the optimum ratio was 1.4:0.6. The specific capacitance increased up to 4 h reaction time because of the large amount of $NiMoO_4.xH_2O$. Due to the benefits of the excellent rate capability of $CoMoO_4$ and the high specific capacitance of $NiMoO_4.xH_2O$, the specific capacitance reached 1039 Fg^{-1} at 2.5 $mAcm^{-2}$. $CoMoO_4$-$NiMoO_4$ nanosheet arrays were grown at various reaction times (2, 4, and 6 h) [102]. The high density of $NiMoO_4$ nanosheets is unfavorable for the diffusion of electrolyte ions, and it may degrade the electrochemical performance. The optimized electrode (4 h) displayed a maximum specific capacitance of 1639.8 Fg^{-1} (3.30 Fcm^{-2}) ever reported for $CoMoO_4$-$NiMoO_4$ structure and excellent cycling stability (95% after 3000 cycles). A facile one-step hydrothermal route was used

to develop NiMoO$_4$/CoMoO$_4$ nanorods [103]. The low internal resistance (R$_b$ = 1.20 Ω), Warburg impedance (1.07 Ω/$\sqrt{}$s), and pseudo charge transfer resistance (R$_{ct}$ = 7.027 Ω) confirmed the enhancement of electrical conductivity, resulting from the synergistic effect of NiMoO$_4$ and CoMoO$_4$ nanorods. At 1 Ag^{-1}, a specific capacitance of 1445 Fg^{-1} was achieved. The rod-like NiMoO$_4$/CoMoO$_4$ nanostructure delivered a specific capacitance of 1164 Fg^{-1} (2 Ag^{-1}) [104]. In NiMoO$_4$-CoMoO$_4$ core/sheath nanowire arrays anchored on NF, the surface of NiMoO$_4$ nanowires was fully wrapped with ultrathin and intersected CoMoO$_4$ nanosheets, resulting in a highly porous structure [105]. The areal capacitance was 5.4 Fcm^{-2} at 2 mAcm^{-2}, and it was preserved up to 3.1 Fcm^{-2} (57.4%) at 40 mAcm^{-2}.

Hierarchical NiMoO$_4$-Co$_3$V$_2$O$_8$ nanorod/nanosphere clusters were prepared by Hu et al. [106]. The redox peaks in CV curves are owing to Ni^{2+}/Ni^{3+} and Co^{2+}/Co^{3+}/Co^{4+}, signifying the reversible non-capacitive Faradaic reactions. Among the prepared samples with different concentrations of Co$_3$V$_2$O$_8$ precursor, the NiMoO$_4$-Co$_3$V$_2$O$_8$-8 composite possessed a large SSA (54.1 m^{2}g^{-1}) with mesoporous structure (pore size~2–10 nm), which could enhance the electrons/ions transport, leading to a maximum specific capacity of 357 Cg^{-1} at 1 Ag^{-1}. The Co$_3$V$_2$O$_8$ nanospheres could accommodate the volume swelling of NiMoO$_4$ nanorods during the long-term cycling process, confirming notable capacity retention of 89.7% over 5000 cycles. Also, the Coulombic efficiency was nearly 100% for each charge/discharge cycle. Honeycomb-like NiMoO$_4$-NiWO$_4$ nanocomposite was hydrothermally grown on NF, and the corresponding SEM images (Figure 3d,e) exhibited plenty of NiWO$_4$ nanoparticles with different particle sizes wrapped on the surface of NiMoO$_4$ nanoflakes [56]. At 2 Ag^{-1}, the composite electrode attained a maximum specific capacitance of 1290 Fg^{-1}. As shown in Figure 3f, cycling stability was 93.1% after 3000 cycles. Sharma et al. [107] experimentally and theoretically investigated Zn-doped NiMoO$_4$-AWO$_4$ (A = Co or Mg) core-shell structure using the density-functional theory method. Even though the MgWO$_4$ (−110) surface is more stable than MgWO$_4$ (−202) due to the lower surface energy, the result of lattice dynamics obviously shows that Zn-NiMoO$_4$-MgWO$_4$ (−110) is dynamically unstable, and MgWO$_4$ is thus incompatible for being a shell for the Zn-NiMoO$_4$ core structure. For Zn-NiMoO$_4$-MgWO$_4$ (−110), the interface interaction was too strong, so that the MgWO$_4$ shell pulled out atoms from the Zn-NiMoO$_4$ surface, resulting in the surface degradation of the Zn-NiMoO$_4$ core. The dynamically stable Zn-NiMoO$_4$-CoWO$_4$ structure improves the ion diffusion, and the interfacial effects are controlled by the Zn dopant and the distinct surface. Therefore, Zn-NiMoO$_4$-CoWO$_4$ showed better performance than Zn-NiMoO$_4$-MgWO$_4$, and the areal capacitance was 7.12 Fcm^{-2} at 2 mAcm^{-2}. The 3D ZnFe$_2$O$_4$-NiMoO$_4$ nanosheet arrays fabricated on rGO/NF substrate exhibited a maximum specific capacitance of 1854 Fg^{-1} at 1 Ag^{-1} for 4 h reaction time [108]. Apart from the above-discussed heterogeneous structures, homogeneous structures (NiMoO$_4$ itself acting as core and shell materials) were also attempted. NiMoO$_4$-NiMoO$_4$ sheet-on-wire nanoarrays displayed good electrochemical performance over the pure NiMoO$_4$ nanowires by eliminating the potential barrier at the nanowire/nanosheet interface [109]. Also, homogeneous NiMoO$_4$-NiMoO$_4$.xH$_2$O nanorods/nanosheets performed well, compared to the pure NiMoO$_4$ nanoarrays, in terms of areal-specific capacitance, rate performance, and cycle life [110].

Table 1. Electrochemical performances of the core-shell structures based on the $NiMoO_4$-metal oxide composite for supercapacitors.

Core-Shell Structure	Role of NiMoO$_4$	Morphology of NiMoO$_4$	Surface Area (m^{2}g^{-1})	Specific Capacity/ Specific Capacitance	Cycling Stability	Rate Capability	Energy-density (Whkg^{-1})	Power-density (Wkg^{-1})	Ref.
MoO$_3$-NiMoO$_4$	shell	nanobelt	26	1307 Fg^{-1} (1 mVs^{-1}) and 748 Fg^{-1} (0.5 Ag^{-1})	171% (10,000 cycles)	186 Fg^{-1} (50 Ag^{-1})	37.5	425	[49]
CuO-NiMoO$_4$	shell	nanowire	-	2600 Fg^{-1} (3.9 Fcm^{-2}) at 3 mAcm^{-2}	87.3% (5000 cycles)	1829.3 Fg^{-1} (40 mAcm^{-2})	42.28	631.57	[50]
SnO$_2$-NiMoO$_4$	shell	nanosheet	90.67	0.65 mAhcm^{-2} (5 mAcm^{-2})	84.2% (5000 cycles)	57.9% (50 mAcm^{-2})	78.4	895	[51]
NiMoO$_4$-MnO$_2$	core	nanowire	-	3.9 Fcm^{-2} (8 mAcm^{-2})	90.5% (4000 cycles)	3.07 Fcm^{-2} (32 mAcm^{-2})	-	-	[52]
NiMoO$_4$-MnO$_2$	core	nanosheet	-	976 Fg^{-1} (1 Ag^{-1})	90.9% (3000 cycles)	732 Fg^{-1} (15 Ag^{-1})	-	-	[53]
α-NiMoO$_4$-δ-MnO$_2$	core	nanorod	-	1136 Fg^{-1} (2 Ag^{-1})	101.9% (5000 cycles)	580 Fg^{-1} (20 Ag^{-1})	-	-	[54]
MnO$_2$-NiMoO$_4$	shell	nanoflake	-	582.2 Fg^{-1} (1 Ag^{-1})	115.5% (5000 cycles)	322.2 Fg^{-1} (10 Ag^{-1})	32.5	750	[55]
NiMoO$_4$-Co$_3$O$_4$	core	nanosheet	-	1722.3 Fg^{-1} (1 Ag^{-1})	91% (6000 cycles)	80.8% (10 Ag^{-1})	37.1	798.0	[58]
Co$_3$O$_4$-MMoO$_4$ (M = Ni)	shell	-	-	2041 Fg^{-1} (0.5 Ag^{-1})	72% (3000 cycles)	1540 Fg^{-1} (8 Ag^{-1})	41.9	298	[59]
Co$_3$O$_4$-NiMoO$_4$	shell	nanosheet	10.28	1526 Fg^{-1} (3 mAcm^{-2})	70% (1000 cycles)	72% (30 mAcm^{-2})	37.8	482	[60]
Co$_3$O$_4$-NiMoO$_4$	shell	nanosheet	251.2	3.61 Fcm^{-2} (3 mAcm^{-2})	77.4% (3000 cycles)	2.96 Fcm^{-2} (15 mAcm^{-2})	-	-	[61]
Co$_3$O$_4$-NiMoO$_4$	shell	nanosheet	-	636.8 Cg^{-1} (5 mAcm^{-2})	84.1% (2000 cycles)	280.2 Cg^{-1} (40 mAcm^{-2})	58.5	389	[62]
Co$_3$O$_4$-NiMoO$_4$	shell	nanosheet	-	3.61 Fcm^{-2} (2 mAcm^{-2})	101.3% (9000 cycles)	44% (30 mAcm^{-2})	-	-	[63]
Co$_3$O$_4$-NiMoO$_4$	shell	nanosheet	-	1476 Fg^{-1} (1 Ag^{-1})	96% (2000 cycles)	1200 Fg^{-1} (20 Ag^{-1})	-	-	[64]
Co$_3$O$_4$-NiMoO$_4$	shell	nanosheet	-	2.3 Fcm^{-2} (1 mAcm^{-2})	80% (4000 cycles)	73% (20 Acm^{-2})	0.249 mWh cm^{-2}	1.6 mW cm^{-2}	[65]

Table 1. *Cont.*

Core-Shell Structure	Role of NiMoO$_4$	Morphology of NiMoO$_4$	Surface Area (m^{2}g^{-1})	Specific Capacity/ Specific Capacitance	Cycling Stability	Rate Capability	Energy-density (Whkg^{-1})	Power-density (Wkg^{-1})	Ref.
Co$_3$O$_4$.NiMoO$_4$	shell	nanosheet	243.4	998.05 Fg^{-1} (0.5 Ag^{-1})	89.9% (3000 cycles)	880 Fg^{-1} (20 Ag^{-1})	-	-	[66]
Co$_3$O$_4$-NiMoO$_4$/ CoMoO$_4$	NiMoO$_4$/ CoMoO$_4$ as shell	nanoflake	253.5	272.2 mAhg^{-1} (1 Ag^{-1})	84.5% (1000 cycles)	114.9 mAhg^{-1} (25 Ag^{-1})	53.9	1000	[67]
NiCo$_2$O$_4$-NiMoO$_4$	shell	nanofilm	-	685.7 Cg^{-1} (1 Ag^{-1})	100% (10000 cycles)	621 Cg^{-1} (10 Ag^{-1})	96.3	4050	[71]
NiCo$_2$O$_4$-NiMoO$_4$	shell	nanosheet	-	5.80 Fcm^{-2} (10 mAcm^{-2})	81.8% (5000 cycles)	4.85 Fcm^{-2} (80 mAcm^{-2})	21.7	157	[72]
NiCo$_2$O$_4$-NiMoO$_4$	shell	nanoflake	121.9	1242 Fg^{-1} (10 mAcm^{-2})	84% (5000 cycles)	987 Fg^{-1} (80 mAcm^{-2})	-	-	[73]
NiCo$_2$O$_4$-NiMoO$_4$	shell	nanosheet	-	1770.95 Cg^{-1} (3 mAcm^{-2})	102.78% (5000 cycles)	1334.18 Cg^{-1} (40 mAcm^{-2})	30.57	676.06	[74]
NiCo$_2$O$_4$-NiMoO$_4$	shell	nanoplate	-	1974 Fg^{-1} (5 mAcm^{-2})	76% (5000 cycles)	1117 Fg^{-1} (100 mAcm^{-2})	47	400	[75]
NiCo$_2$O$_4$-NiMoO$_4$	shell	nanosheet	-	2806 Fg^{-1} (5 Ag^{-1})	87.7% (5000 cycles)	1408 Fg^{-1} (30 Ag^{-1})	64.2	750	[76]
NiCo$_2$O$_4$-NiMoO$_4$	shell	nanosheet	91.97	2.917 Fcm^{-2} (2 mAcm^{-2})	90.6% (2000 cycles)	1.608 Fcm^{-2} (40 mAcm^{-2})	-	-	[77]
NiCo$_2$O$_4$-NiMoO$_4$	shell	nanosheet	NiCo$_2$O$_4$-NiMoO$_4$/ NF = 70.06 NiCo$_2$O$_4$-NiMoO$_4$/ CC = 74.34	NF = 1.294 Fcm^{-2} CC = 0.443 Fcm^{-2} (50 mVs^{-1})	80% (3000 cycles)	-	NF = 11.90 CC = 5.06	800	[78]
NiCo$_2$O$_4$-NiMoO$_4$	shell	nanosheet	100.3	2474 Fg^{-1} (1 Ag^{-1})	95% (1000 cycles)	2080 Fg^{-1} (20 Ag^{-1})	42.1	175	[79]
NiCo$_2$O$_4$-NiMoO$_4$	shell	nanoflake	-	6.29 Fcm^{-2} (5 mAcm^{-2})	87% (5000 cycles)	3.58 Fcm^{-2} (100 mAcm^{-2})	-	-	[80]
NiCo$_2$O$_4$-NiMoO$_4$	shell	nanosheet	-	7.29 Fcm^{-2} (2 mAcm^{-2})	82.2% (5000 cycles)	84.1% (60 mAcm^{-2})	52.6	332.4	[81]
NiCo$_2$O$_4$-NiMoO$_4$	shell	nanosheet	30.56	2522 mFcm^{-2} (1 mAcm^{-2})	89.8% (5000 cycles)	-	53.3	750	[82]

Table 1. *Cont.*

Core-Shell Structure	Role of NiMoO$_4$	Morphology of NiMoO$_4$	Surface Area (m^{2}g^{-1})	Specific Capacity/ Specific Capacitance	Cycling Stability	Rate Capability	Energy-density (Whkg^{-1})	Power-density (Wkg^{-1})	Ref.
NiCo$_2$O$_4$-NiMoO$_4$	shell	nanosheet	NiCo$_2$O$_4$-NiMoO$_4$/NF = 14.52 (NH$_4$F) NiCo$_2$O$_4$-NiMoO$_4$/CC = 74.34 (urea)	NiCo$_2$O$_4$-NiMoO$_4$/NF = 4.05 Fcm^{-2} (NH$_4$F) NiCo$_2$O$_4$-NiMoO$_4$/CC = 1.62 Fcm^{-2} (urea)	NiCo$_2$O$_4$-NiMoO$_4$/NF = 80% (5000 cycles) (NH$_4$F)	-	70.78	3250	[83]
NiCo$_2$O$_4$-NiMoO$_4$	shell	nanoparticle	-	3705 Fg^{-1} (1.5 Ag^{-1})	94.6% (5000 cycles)	3525 Fg^{-1} (30 Ag^{-1})	76.45	370	[84]
NiCo$_2$O$_4$-NiMoO$_4$/rGO	shell	nanoflake	79.7	9.41 Fcm^{-2} (10 mAcm^{-2})	75% (2000 cycles)	6.02 Fcm^{-2} (50 mAcm^{-2})	-	-	[85]
NiMoO$_4$-NiCo$_2$O$_4$	core	honeycomb nanostructure	-	2695 Fg^{-1} (20 mAg^{-2})	98.9% (3000 cycles)	1527 Fg^{-1} (28 mAg^{-2})	61.2	371.5	[86]
rZnCo$_2$O$_4$-NiMoO$_4$·H$_2$O	shell	nanosheet	-	3.53 Fcm^{-2} (1 mAcm^{-2})	95.4% (5000 cycles)	-	2.55 mWhcm^{-3}	0.033 Wcm^{-3}	[88]
ZnCo$_2$O$_4$-NiMoO$_4$	shell	nanosheet	156.52	1480.48 Fg^{-1} (2 mAcm^{-2})	90.6% (15000 cycles)	959.04 Fg^{-1} (50 mAcm^{-2})	48.6	2820	[89]
ZnCo$_2$O$_4$-NiMoO$_4$	shell	nanosheet	-	1912 Fg^{-1} (1 Ag^{-1})	84.1% (10000 cycles)	1040 Fg^{-1} (20 Ag^{-1})	57.5	900	[90]
ZnCo$_2$O$_4$-NiMoO$_4$	shell	nanosheet	-	1238.1 Cg^{-1} (3 mAcm^{-2})	103.4% (5000 cycles)	932.8 Cg^{-1} (40 mAcm^{-2})	25.3	787.9	[91]
CuCo$_2$O$_4$-NiMoO$_4$	shell	nanosheet	-	2207 Fg^{-1} (1.25 Ag^{-1})	95.6% (5000 cycles)	1560.35 Fg^{-1} (25 Ag^{-1})	40	-	[92]
CuCo$_2$O$_4$-NiMoO$_4$	shell	nanosheet	-	276 mAhg^{-1} (1 Ag^{-1})	98.3% (8000 cycles)	133 mAhg^{-1} (10 Ag^{-1})	44.8	374.2	[93]
MnCo$_2$O$_4$-NiMoO$_4$	shell	nanosheet	119.2	1244 Fg^{-1} (1 Ag^{-1})	81% (2500 cycles)	1132 Fg^{-1} (10 Ag^{-1})	42	852.3	[94]
MnCo$_2$O$_4$-NiMoO$_4$	shell	nanoflake	-	1718 Fg^{-1} (1 Ag^{-1})	84% (6000 cycles)	1200 Fg^{-1} (8 Ag^{-1})	42.3	797	[95]
MgCo$_2$O$_4$-NiMoO$_4$	shell	nanosheet	-	1775 Fg^{-1} (1 Ag^{-1})	74.7% (5000 cycles)	1191 Fg^{-1} (20 Ag^{-1})	37.5	480	[96]
MgCo$_2$O$_4$-MMoO$_4$ (M = Ni)	shell	nanosheet	-	1111.57 Cg^{-1} (1 mAcm^{-2})	90.04% (5000 cycles)	788.09 Cg^{-1} (20 mAcm^{-2})	23.46	102.6	[97]

Table 1. *Cont.*

Core-Shell Structure	Role of NiMoO$_4$	Morphology of NiMoO$_4$	Surface Area (m^{2}g^{-1})	Specific Capacity/ Specific Capacitance	Cycling Stability	Rate Capability	Energy-density (Whkg^{-1})	Power-density (Wkg^{-1})	Ref.
NiCoMn-O -NiMoO$_4$-C	shell	nanolayer	-	2189.5 Fg^{-1} (0.25 Ag^{-1})	81.6% (1500 cycles)	1361.1 Fg^{-1} (20 Ag^{-1})	59.9	214.1	[98]
ZnNiCo-O- NiMoO$_4$	shell	nanowire/ nanosheet	185	338.5 mAhg^{-1} (3 mAcm^{-2})	86% (10,000 cycles)	71% (25 mAcm^{-2})	35.3	5115.1	[99]
CoMoO$_4$- NiMoO$_4 \cdot x$H$_2$O	shell	nanosheet	100.79	1582 Fg^{-1} (1 Ag^{-1})	97.1% (3000 cycles)	1050 Fg^{-1} (15 Ag^{-1})	41.8	700	[100]
CoMoO$_4$- NiMoO$_4.x$H$_2$O	shell	nanorod	17.0	1039 Fg^{-1} (2.5 mAcm^{-2})	75.1% (1000 cycles)	750 Fg^{-1} (100 mAcm^{-2})	-	-	[101]
CoMoO$_4$-NiMoO$_4$	shell	nanosheet	31.77	1639.8 Fg^{-1} (10 mAcm^{-2})	95% (3000 cycles)	1106.9 Fg^{-1} (60 mAcm^{-2})	28.7	267	[102]
NiMoO$_4$-CoMoO$_4$	core	nanorod	-	1445 Fg^{-1} (1 Ag^{-1})	78.8% (3000 cycles)	815 Fg^{-1} (10 Ag^{-1})	-	-	[103]
NiMoO$_4$-CoMoO$_4$	core	nanorod	-	1164 Fg^{-1} (2 Ag^{-1})	75% (3000 cycles)	974 Fg^{-1} (20 Ag^{-1})	23.1	375	[104]
NiMoO$_4$-CoMoO$_4$	core	nanowire	-	5.4 Fcm^{-2} (2 mAcm^{-2})	82.6% (8000 cycles)	3.1 Fcm^{-2} (40 mAcm^{-2})	49.3	630	[105]
NiMoO$_4$-Co$_3$V$_2$O$_8$	core	nanorod	54.1	357 Cg^{-1} (1 Ag^{-1})	89.7% (5000 cycles)	77.8% (5 Ag^{-1})	48.5	839.1	[106]
NiMoO$_4$-NiWO$_4$	core	nanoflake	-	1290 Fg^{-1} (2 Ag^{-1})	93.1% (3000 cycles)	101.3 Fg^{-1} (18 Ag^{-1})	-	-	[56]
Zn-doped NiMoO$_4$-AWO$_4$ (A = Co or Mg)	Zn-doped NiMoO$_4$ core	nanoneedle	-	6.41 Fcm^{-2} (Zn-NiMoO$_4$-MgWO$_4$) 7.12 Fcm^{-2} (Zn-NiMoO$_4$-CoWO$_4$) at 2 mAcm^{-2}	96% (1000 cycles)	-	-	-	[107]
ZnFe$_2$O$_4$-NiMoO$_4$	shell	nanosheet	-	1854 Fg^{-1} (1 Ag^{-1})	91.6% (7000 cycles)	1220 Fg^{-1} (20 Ag^{-1})	58.6	799	[108]
NiMoO$_4$-NiMoO$_4$	core/ shell	nanowire/nanosheet	33.2	413 mAhg^{-1} (1 Ag^{-1})	361.2 mAhg^{-1} (3000 cycles)	220 mAhg^{-1} (20 Ag^{-1})	47.2	1380	[109]
NiMoO$_4$- NiMoO$_4.x$H$_2$O	NiMoO$_4$ as core NiMoO$_4.x$H$_2$O as shell	NiMoO$_4$ as nanorod and NiMoO$_4.x$H$_2$O as nanosheet	-	6.34 Fcm^{-2} (4 mAcm^{-2})	89% (5000 cycles)	3.13 Fcm^{-2} (70 mAcm^{-2})	141 mWhcm^{-2}	0.38 mWcm^{-2}	[110]

4.2. NiMoO$_4$-Metal Hydroxide Composite

Transition metal hydroxides are deemed promising candidates for supercapacitor electrodes. The core material with rod-like morphology is very appropriate for designing core-shell nanostructures. Besides, poor crystallinity is more auspicious for ion transport and beneficial for good electrochemical performance [24,111,112]. NiMoO$_4$-Ni(OH)$_2$ nanorods were successfully constructed on NF via hydrothermal and electrodeposition processes [113]. The Ni(OH)$_2$ nanosheets were uniformly covered on the surface of NiMoO$_4$ nanorods in such a way that they were aligned with their planes more or less perpendicular to NiMoO$_4$ nanorods. The nonlinearity of the galvanostatic charge/discharge curves in the voltage range of 0–0.4 V indicates the Faradaic process, and a high value of areal capacitance of 7.43 Fcm^{-2} at 4 mAcm^{-2} is due to the quasi-reversible electron transfer process. NiMoO$_4$-Co(OH)$_2$ nanowire arrays were grown on NF via hydrothermal and electrochemical deposition routes [114]. As displayed in Figure 5a–c, ultrathin Co(OH)$_2$ nanoflakes (thickness~10–20 nm) were uniformly wrapped on NiMoO$_4$ nanowires, due to which the areal capacitance reached 2.335 Fcm^{-2} at 5 mAcm^{-2}, and capacitance retention rate was 83% after 5000 cycles. Such a good performance is due to the large surface area of Co(OH)$_2$ and open space that enables the rapid intercalation/deintercalation of ions by affording abundant active sites. The NiMoO$_4$-Co(OH)$_2$ produces more ion migration channels and facilitates the electrolyte ion transport in 3D space, as displayed in Figure 5d. The large electroactive surface area of the electrode is confirmed by low R$_{ct}$ (Faradaic interfacial charge transfer resistance) from EIS measurement, and the value increases after 5000 cycles, which is probably due to the loss of some active material and the corrosion of NF caused by the dissolved oxygen in KOH electrolyte.

Layered double hydroxides (LDHs) are a group of materials in which the layers contain divalent (M^{2+}) and trivalent (M^{3+}) metal ions, and the interlayer region is occupied by charge-balancing anions. Their advantages include large interlayer spacing, high surface area, and easy synthesis [115]. Ni-Co LDHs are commonly applied with NiMoO$_4$ nanosheets owing to their high theoretical capacitance (>3000 Fg^{-1}) and low cost [116]. To construct NiMoO$_4$-Ni-Co LDH-NiCo$_2$O$_4$ nanorod/nanosheet structure, NiCo$_2$O$_4$ nanorods were hydrothermally prepared on NF, and then Ni-Co LDH nanosheets were grown on NiCo$_2$O$_4$ by electrodeposition [117]. Afterward, Ni-Co LDH was utilized as a template to provide a larger area for the NiMoO$_4$ nanosheet growth. The size and thickness of nanosheets were controlled by varying the electrodeposition time (50, 100, 150, and 200 s). The NiMoO$_4$-Ni-Co LDH shell protects the NiCo$_2$O$_4$ core from structural damage and further improves material stability as well as capacity. A maximum specific capacity of 1035 Cg^{-1} was attained by NiMoO$_4$-Ni-Co LDH150-NiCo$_2$O$_4$. Hydrothermal synthesis of Ni-Co LDH-NiMoO$_4$/GO on carbon fiber is illustrated in Figure 5e [116]. The graphene oxide (GO) layer was attached with Ni-Co LDH-NiMoO$_4$ by physical adsorption. The surface of GO contains more oxygen-containing functional groups, and the carbon fiber is adsorbed with GO to create a stable 3D framework. As evident from the XRD pattern in Figure 5f, the Ni-Co LDH is a mixture of rhombohedral Ni(OH)$_2$ and Co(OH)$_2$. The poor crystallinity of NiMoO$_4$ is due to the presence of many pores. Figure 5g shows the resistance properties of Ni-Co LDH-Ni-MoO$_4$ and Ni-Co LDH-NiMoO$_4$/GO, investigated by EIS measurements. It is clear that the R$_s$ value of the Ni-Co LDH-NiMoO$_4$/GO (6.79 Ω) electrode is less compared to Ni-Co LDH-NiMoO$_4$ (9.21 Ω). Therefore the former electrode exhibited good performance in all aspects. Double-shell hierarchical structure of P-doped cobalt carbonate hydroxide-NiMoO$_4$ (P-CoCH-NiMoO$_4$) was constructed through hydrothermal growth of densely-packed NiMoO$_4$ nanosheets on NF, followed by the growth of CoCH nanowires [118]. Afterward, in-situ vapor phase P-doping was applied to change the crystal structure and surface heteroatoms distribution of the composite. The large mass loading of active material supports the energy storage capacity and electrochemically active sites. The unique structure with porous gradient channels and hydrophilic nature can increase the electrolyte permeation and ion diffusion efficiency. The conductive NiMoO$_4$ arrays can facilitate the electron transfer between NF and P-CoCH. Besides, due to the

phosphorization process, lattice distortion, surface defects, and oxygen vacancies were introduced on the surface of CoCH nanowires, which can efficiently increase the electron transfer and create additional catalytic active sites. Owing to these facts, the as-prepared electrode reached a high areal capacitance (5.08 Fcm^{-2} at 2 $mAcm^{-2}$) and good cycling stability (82.7% after 2000 cycles).
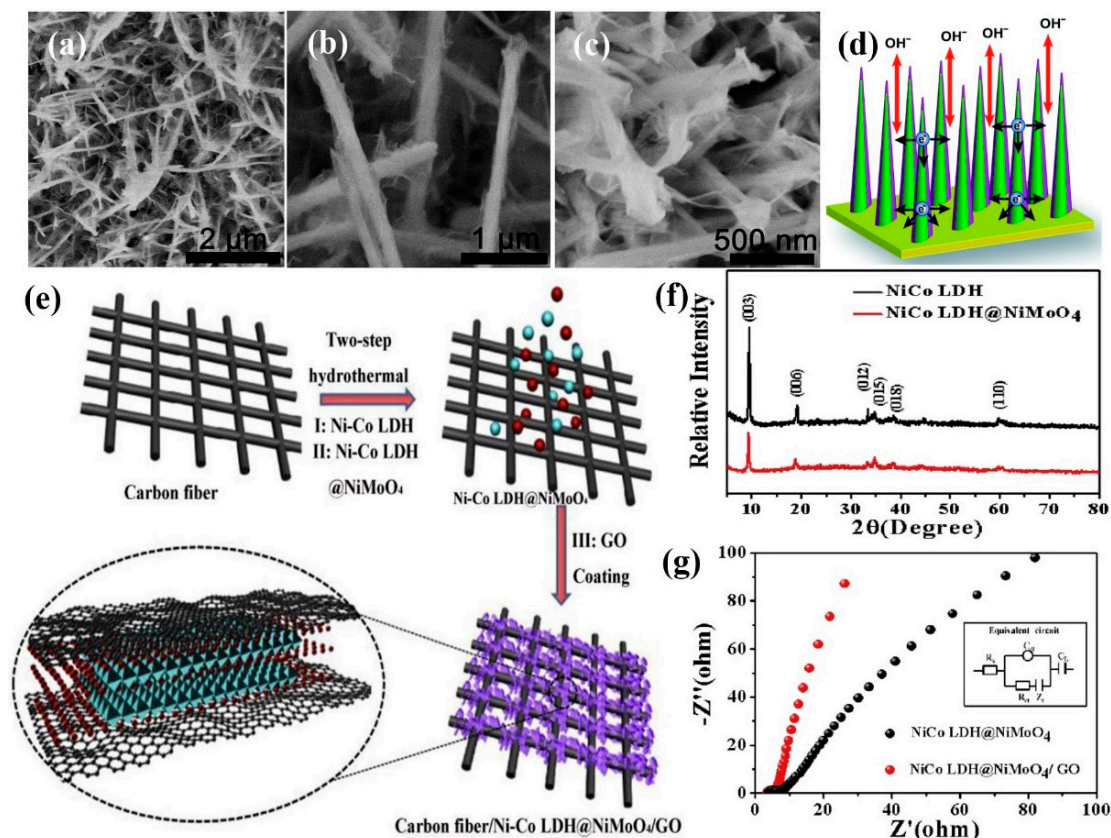

Figure 5. (**a**–**c**) High magnification SEM images of $NiMoO_4−Co(OH)_2$ nanowires on NF, (**d**) Schematic diagram of the high−performance of $NiMoO_4−Co(OH)_2$ [114]. Reproduced from Ref. [114] with permission from The Royal Society of Chemistry, 2015. (**e**) The synthesis process of Ni−Co LDH−$NiMoO_4$/GO on carbon fiber, (**f**) XRD patterns of Ni−Co LDH and Ni−Co LDH−$NiMoO_4$ samples, (**g**) EIS of the Ni−Co LDH−$NiMoO_4$ and Ni−Co LDH−$NiMoO_4$/GO electrodes [116]. Reproduced from Ref. [116] with permission from Elsevier, 2019.

4.3. NiMoO₄-Metal Chalcogenide Composite

A common issue with metal oxides is their limited electron transport. Metal sulfides are recently found to have improved performance owing to their diversified crystal structure, high electrical conductivity, and good electrochemical activity of sulfur than oxygen [119,120]. The electrochemical performance of $NiMoO_4$-metal hydroxide, $NiMoO_4$-metal chalcogenide, $NiMoO_4$-carbon material, and $NiMoO_4$-conductive polymer core-shell structures is shown in Table 2. Funnel-shaped $NiMoO_4$-Co_3S_4/NF nanostructure was synthesized using different hydrothermal reaction times (8, 12, and 16 h) and electrochemical deposition [121]. The SEM images revealed that 2D $NiMoO_4$ nanosheets have sufficient open space and large lateral size, which are beneficial to the deposition of Co_3S_4. The Co_3S_4 nanosheets were uniformly deposited over the $NiMoO_4$ porous structure by tight interconnection and arranged in the same orientation with $NiMoO_4$, forming a double-layer open-up network (Figure 6a,b). Consequently, this improves electrolyte penetration and charge transport. As shown in Figure 6c, the closed region of the cyclic voltammetry (CV) curve of $NiMoO_4$-Co_3S_4 (12 h) is larger than that of the pure $NiMoO_4$ and Co_3S_4. Therefore, the ultrathin architecture offered a large specific capacitance of 359.31 $mAhg^{-1}$ (2589.6 Fg^{-1})

at 0.5 Ag^{-1}. This great improvement was due to the parallel orientation of $NiMoO_4$ and Co_3S_4 nanosheets. In $NiMoO_4$-MoS_2 nanorods, the pseudocapacitive property arises due to the redox reactions of Ni^{2+}/Ni^{3+} from $NiMoO_4$ and Mo^{4+} ions from MoS_2 [122]. The heterostructure electrode offered an outstanding specific capacitance of 2246.7 Fg^{-1} at 1 Ag^{-1} and improved cycling stability (88.4% after 5000 cycles). In the high-frequency region of Nyquist plots, the charge transfer resistance (R_{ct}) value of $NiMoO_4$-MoS_2 (1.24 Ω) is relatively smaller compared to $NiMoO_4$ (2.77 Ω) and MoS_2 (4.81 Ω), which is due to the rapid electron transport between $NiMoO_4$-MoS_2 nanorods and KOH electrolyte. In the low-frequency region, the $NiMoO_4$-MoS_2 electrode shows a larger slope compared to $NiMoO_4$ and MoS_2, implying a lower diffusion resistance. This is ascribed to a highly porous structure with mesopores and macropores, enabling more active sites. The ASC device composed of $NiMoO_4$-MoS_2 as cathode and N, S-codoped porous carbon as anode delivered a high energy-density of 47.5 $Whkg^{-1}$ at a power-density of 440 Wkg^{-1}.
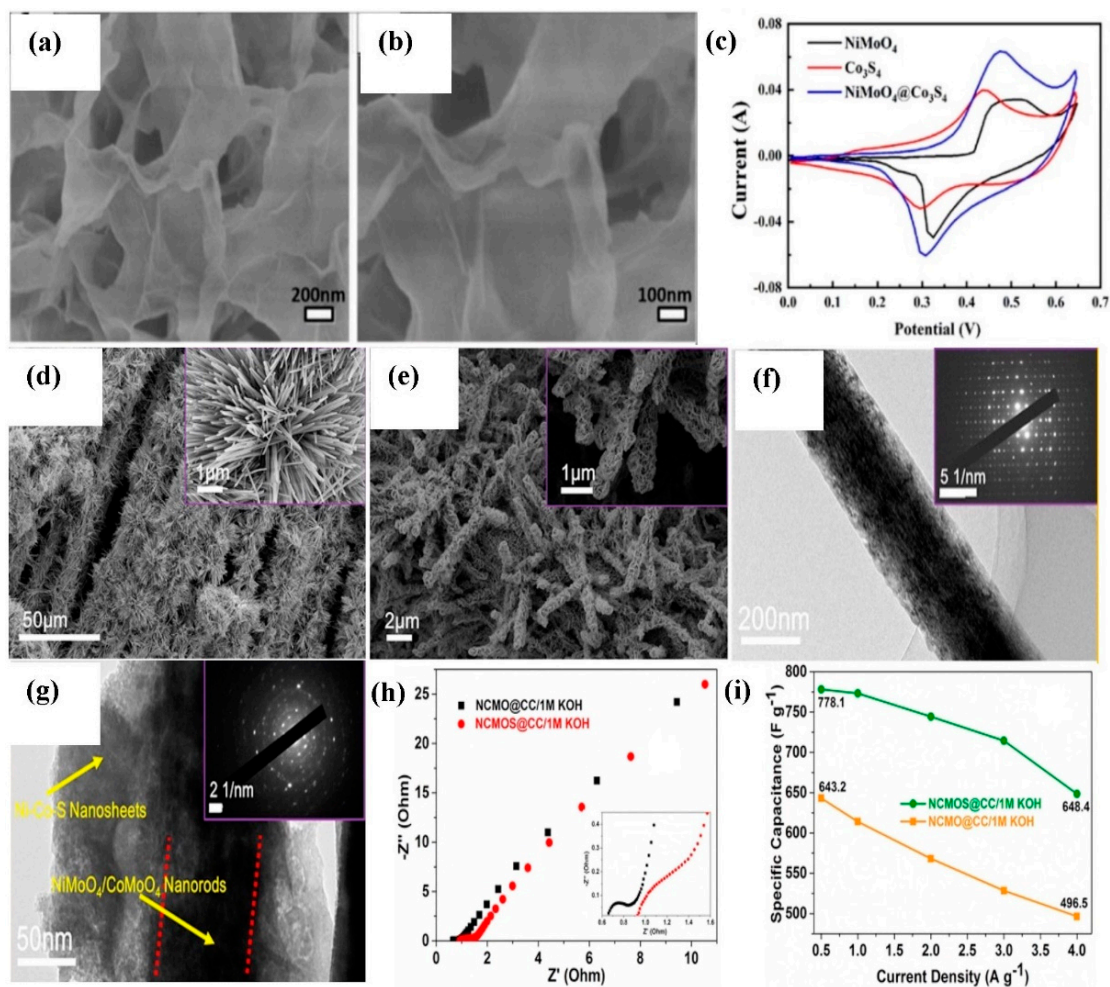

Figure 6. (**a**,**b**) SEM images of $NiMoO_4$−Co_3S_4 nanosheets on NF, (**c**) CV curves of $NiMoO_4$ (12 h), Co_3S_4 and $NiMoO_4$−Co_3S_4 electrodes at 10 mVs^{-1} scan rate [121]. Reproduced from Ref. [121] with permission from Elsevier, 2022. (**d**,**e**) SEM images, (**f**,**g**) TEM images (inset: SAED patterns), (**h**) Nyquist plots for NCMO/CC and NCMOS/CC, (**i**) Variation of mass−specific capacitance over current density for NCMO/CC and NCMOS/CC [123]. Reproduced from Ref. [123] with permission from Elsevier, 2019.

The 3D $NiMoO_4$-Ni_3S_2 heterostructure was made up of numerous Ni_3S_2 nanosheets wrapped on $NiMoO_4$ nanorods [124]. This unique morphology helps to effectively inhibit the volume change of the electrode material during the long-term cycle process. The abundant pore channels can reduce the transmission and diffusion path of ions. Additionally,

the intrinsic resistance (IR drop) of the electrode is small. Because of these reasons, the areal capacitance reached 2.3 Fcm^{-2} at 1 $mAcm^{-2}$ (1.8 times larger than that of $NiMoO_4$). The 1D Ni_3S_2-$NiMoO_4$ structure exhibited a high areal capacity of 1327.3 $\mu Ahcm^{-2}$ at 2 $mAcm^{-2}$ and a rate capability of 67.8% (900.9 $\mu Ahcm^{-2}$ at 40 $mAcm^{-2}$) [125]. The hair-like Ni_3S_2 nanowires provided high electrical conductivity and inhibited the aggregation of $NiMoO_4$ nanosheets. Hence, Ni_3S_2-$NiMoO_4$ (diameter~150 nm) nanowires exhibited good cycling stability (96.7% after 6000 cycles). $NiMoO_4$-NiS_2/MoS_2 (S-$NiMoO_4$-x) nanocomposite was developed via in-situ sulfurization [sulfur with the mass ratio of 1:x (x = 1, 2, and 3)] of the hydrothermally-prepared $NiMoO_4$ nanowires [126]. The S-$NiMoO_4$-2 exhibited good performance (970 Fg^{-1} at 5 Ag^{-1}) due to the porous structure and the long-range continuous interfaces between outer NiS_2/MoS_2 nanosheets and inner $NiMoO_4$ nanowires, which offers more accessible sites and fast charge transfer channels. $NiMoO_4$-Ni_9S_8/MoS_2 nanorods were constructed using hydrothermal-assisted direct sulfurization [127]. The hierarchical porous structure is a combination of both micropores and mesopores contributed by outer Ni_9S_8/MoS_2 nanoflakes and inner $NiMoO_4$ nanorods, respectively, due to the introduction of sulfur during the calcination process. Because of the high porosity and synergistic effect of bimetal sulfides, the specific capacity attained a maximum of 488.9 Fg^{-1} at 1 Ag^{-1}. The 1D core-double shell arrays of $NiMoO_4$-C-Ni_3S_2 were prepared on NF by successively using hydrothermal, carbonization and electrodeposition processes [128]. The order of capacitive responses was $NiMoO_4$-C-Ni_3S_2 > $NiMoO_4$-Ni_3S_2 > $NiMoO_4$ > $NiMoO_4$-C for 50 mVs^{-1} scan rate in CV measurement. The reason for less capacitance after carbon coating is that the carbon layer covers the active sites of $NiMoO_4$. $NiMoO_4$-C-Ni_3S_2 shows a larger capacitance compared to $NiMoO_4$-Ni_3S_2 because the inner shell of carbon helps to strengthen the linkage between the $NiMoO_4$ core nanowire and Ni_3S_2 outer shell, which can eliminate the interfacial resistance and load a large amount of Ni_3S_2 nanosheets. The specific capacity reached 7.9 Fcm^{-2} at 5 $mAcm^{-2}$.

Binary metal sulfides usually have richer redox reactions and better conductivity compared to single metal sulfides, showing improved electrochemical performance. Among them, $NiCo_2S_4$ nanostructure is the most extensively studied material with $NiMoO_4$ due to its superior ion transfer rate and rapid electrochemical response. $NiCo_2S_4$-$NiMoO_4$.xH_2O nanoneedle arrays were developed on NF using hydrothermal and sulfur anion exchange processes [129]. $NiCo_2S_4$ nanoneedles served as the backbone for the $NiMoO_4$.xH_2O nanosheet growth. This could increase the conductivity between $NiCo_2S_4$ and $NiMoO_4$ and also efficiently reduce the agglomeration of $NiMoO_4$.xH_2O nanosheets, enabling abundant electroactive sites for redox reactions. Consequently, a specific capacity of 830.2 Fg^{-1} was attained at 2 Ag^{-1}. $NiCo_2S_4$-$NiMoO_4$ nanosheet arrays were constructed by rationally growing $NiCo_2S_4$ nanosheets on NF by anion exchange reaction with Na_2S, followed by decorating with porous $NiMoO_4$ nanosheets [130]. With the increasing reaction time (2, 4, and 6 h), plenty of $NiMoO_4$ nanosheets coated over $NiCo_2S_4$, forming thick $NiCo_2S_4$-$NiMoO_4$ nanosheets with enlarged surface area for fast Faradaic redox reactions. The specific capacitance reached 1487.6 Fg^{-1} at 1 Ag^{-1} for 4 h reaction time. $NiCo_2S_4$-$NiMoO_4$ nanoarrays were fabricated by developing grass-like $NiCo_2S_4$ nanotubes covered by abundant interlinked $NiMoO_4$ nanosheets [131]. At 5 $mAcm^{-2}$, the specific capacitance reached a higher value of 2006 Fg^{-1} compared to bare $NiCo_2S_4$ (1264 Fg^{-1}). To construct $NiCo_2S_4$-$NiMoO_4$ nanospheres, $NiCo_2S_4$ nanoballs were synthesized first [132]. Diethanolamine was used as a weak alkali precipitant that caused the slow reaction rate to favor nucleation and growth. At 1 Ag^{-1}, a maximum specific capacitance of 1714 Fg^{-1} was achieved. $NiCo_2S_4$-$NiMoO_4$ nanostructures were prepared by developing ultrathin, mesoporous, and interconnected $NiMoO_4$ nanosheets on the surface of $NiCo_2S_4$ nanotubes [133]. The areal capacity was 673.3 $\mu Ahcm^{-2}$ at 5 $mAcm^{-2}$. $NiCo_2O_xS_y$-$NiMoO_4$ nanotube/nanosheet structure was hydrothermally grown by Chiu et al. [134]. Ni-Co LDH nanowires were calcined to form $NiCo_2O_4$ nanowires, which were further transformed into $NiCo_2S_4$ core nanotube arrays. $NiCo_2S_4$ is dissolved to form $NiCo_2O_xS_y$ nanotubes during the $NiMoO_4$ shell growth. The nanoparticle-assembled wall of the $NiCo_2O_xS_y$ nanotubes has a large active surface area

for enabling more redox reactions with the electrolyte. Hence, a high specific capacity of 168.18 mAhg^{-1} was gained at 10 mAcm^{-2}.

NiMoO$_4$-Ni-Co-S nanorods were constructed by adopting hydrothermal for NiMoO$_4$ growth [135]. Then, Ni-Co-S was electrodeposited under a scan rate of 5 mVs^{-1} for 6, 8, and 10 cycles. The electrode showed good performance (1892 Fg^{-1} at 5 mAcm^{-2}) for 8 cycles. Single-crystalline NiMoO$_4$/CoMoO$_4$ nanorods enclosed by polycrystalline Ni-Co-S nanosheets (NCMOS) were effectively deposited on CC using the hydrothermal method and electrochemical deposition [123]. After the hydrothermal method, the 3D textile structure of NiMoO$_4$/CoMoO$_4$ (NCMO) was maintained, as shown in Figure 6d. The NCMO nanorods radially grow on CC and form a flower-like structure. As shown in Figure 6e, Ni-Co-S nanosheets create the NCMO surface more wrinkled, which increases the contact area with electrolyte and helps to improve the electrochemical performance. The average diameter of NCMO nanorods is~210 nm, and the TEM image of NCMOS confirmed that nanorods are covered by nanosheets (Figure 6f,g). The bulk solution resistance (R$_s$) and charge transfer resistance (R$_{ct}$) values of NCMOS/CC are higher (0.92, 0.19 Ω) when compared to NCMO/CC (0.63, 0.08 Ω) due to the more loading of active material, as evident from Figure 6h. The NCMOS material exhibited a good specific capacitance of 778.1 Fg^{-1} at 0.5 Ag^{-1} and an excellent rate capability of 648.4 Fg^{-1} at 4 Ag^{-1} (Figure 6i). A flexible ASC was further fabricated with NCMOS and AC, delivering an energy-density of 33.1 WhKg^{-1} at a power-density of 199.6 Wkg^{-1}. Acharya and co-workers [136] scrupulously designed a hollow-tubular rGO-NiMoO$_4$-Ni-Co-S hybrid nanostructure in a fashionable way. First, NiMoO$_4$ nanorods were prepared on rGO-coated NF using a facile hydrothermal method. Next, the as-coated NF was simply dipped into the Co-precursor solution containing 2-methylimidazole to obtain rGO-NiMoO$_4$-Co-MOF (metal-organic framework). This Co-MOF (ZIF-67) was then modified into rGO-NiMoO$_4$-Ni-Co-LDH via an etching process in a Ni-precursor solution. At last, the synthesized material was used for the sulfidation process in thioacetamide to obtain rGO-NiMoO$_4$-Ni-Co-S architecture. The specific capacity reached 318 mAhg^{-1} at 1 Ag^{-1}, and cycling stability was 88.87% (after 10,000 cycles). Moreover, the fabricated rGO-NiMoO$_4$-Ni-Co-S//rGO-MDC (MOF-derived carbon) ASC device delivered an energy-density of 57.24 Whkg^{-1} at a power-density of 801.8 Wkg^{-1} with a notable life span of 90.89% after 10,000 cycles.

Metal selenides have a lower band gap than the corresponding sulfide compounds. Therefore, very recently, the Ni-Co-Se-NiMoO$_4$ hybrid structure was developed on rGO-coated NF [137]. As shown in Figure 7a, first, porous Ni-Co-Se nanorods were vertically deposited on an rGO-NF substrate via oxalic acid template and selenization processes. Then, the surface of Ni-Co-Se nanorods was decorated with hydrothermally-prepared NiMoO$_4$ nanosheets to attain a Ni-Co-Se-NiMoO$_4$ structure with a high SSA (114 m^{2}g^{-1}) and pore volume (0.42 cm^{3}g^{-1}). As shown in Figure 7b,c, hollow Ni-Co-Se nanorods interconnect with NiMoO$_4$ nanosheets, which leads to the Ni-Co-Se-NiMoO$_4$-rGO-NF structure. The as-prepared electrode shows a magnificent electrochemical performance in terms of a maximum specific capacity of 396.1 mAhg^{-1} at 1 Ag^{-1} and excellent capacity retention of 87.6% after 8000 cycles (Figure 7d,f). As illustrated in Figure 7e, the diffusion-controlled current contribution is leading at a low scan rate. With increasing scan rate, the capacitive contribution increases, enhancing the interaction of electrolyte ions towards the electrode surface. An HSC was assembled by sandwiching the battery-type electrode with an EDLC-type OA-MOF-PCCNT-NF electrode (oxalic acid and MOF-derived porous carbon/CNT coated NF). The device showed a high energy-density of 63.1 Whkg^{-1} at a power-density of 799.8 Wkg^{-1}, along with 89.4% capacitance retention after 8000 cycles. The 1D-NiMoO$_4$-2D-NiMoS$_4$ (NMS) porous nanostructure was designed by growing NiMoO$_4$ nanorods first and then treating it with Na$_2$S solution at different concentrations (5, 10, and 20 mM) [138]. When the S$_2^-$ concentration increased to 20 mM, NiMoO$_4$ nanorods dissolved into nanoparticles and agglomerated into clumps. Because of this structural collapse, the surface area decreased, and hence the electrochemical performance became poor. The porous structure of NMS-10 mainly consists of mesopores, macropores, and a

few micropores. The mesopores and micropores existed on $NiMoO_4$ nanorods and $NiMoS_4$ nanosheets, while the macropores were due to the staggering growth of $NiMoS_4$ nanosheets. The NMS-10 produced a maximum specific capacitance of 832.3 Fg^{-1} at 5 Ag^{-1}.
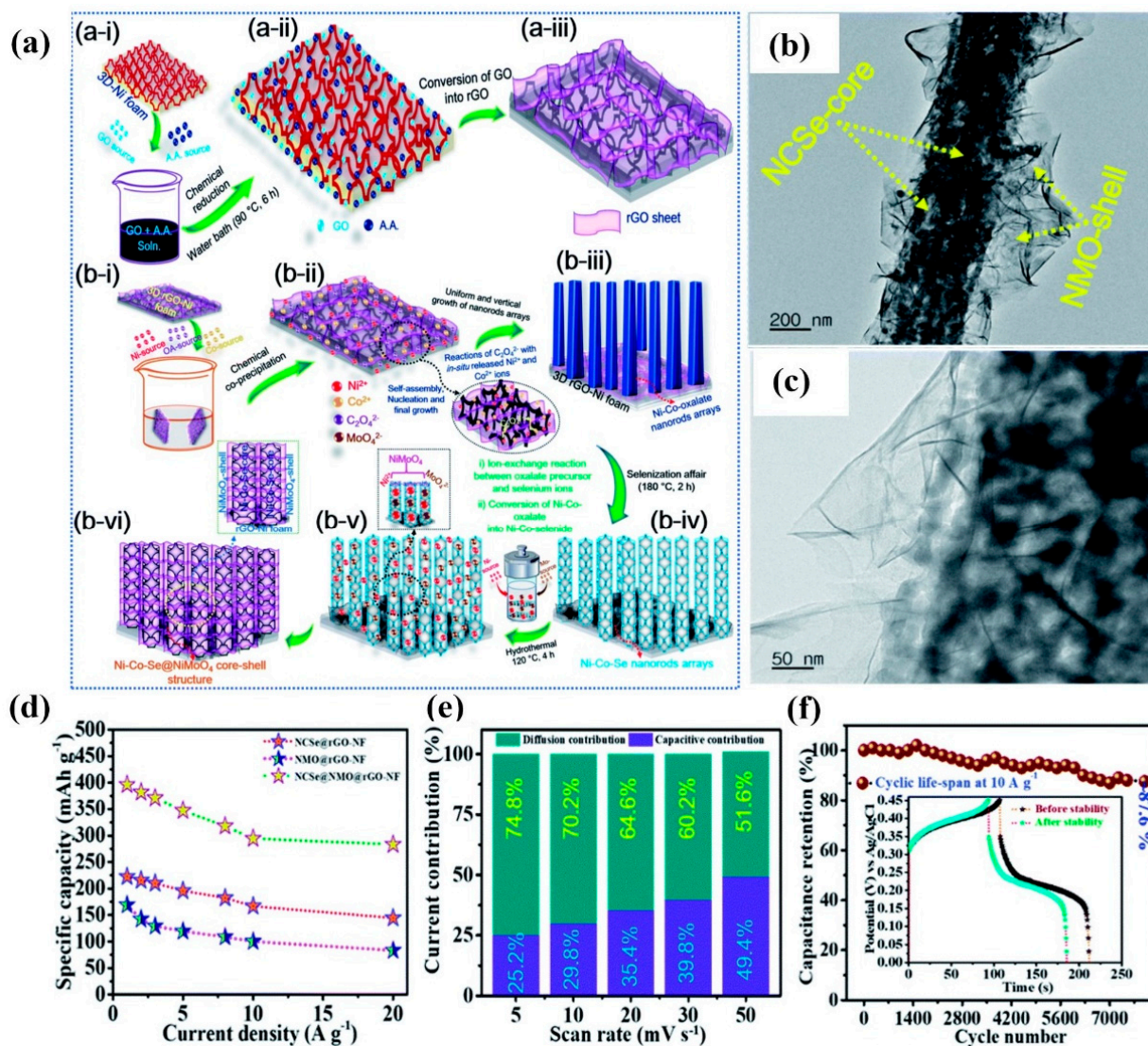
Figure 7. (**a**) Schematic diagram of the synthesis of the $Ni-Co-Se-NiMoO_4-rGO-NF$, (**b**,**c**) TEM images, (**d**) rate capability curves, (**e**) diffusion and capacitive current contributions, and (**f**) cycling performance at 10 Ag^{-1} [137]. Reproduced from Ref. [137] with permission from The Royal Society of Chemistry, 2022.

Table 2. Electrochemical performances of core-shell structures using composites of $NiMoO_4$-metal hydroxide, $NiMoO_4$-metal chalcogenide, $NiMoO_4$-carbon material, $NiMoO_4$-conductive polymer for supercapacitors.

Core-Shell Structure	Role of $NiMoO_4$	Morphology of $NiMoO_4$	Surface Area (m^2g^{-1})	Specific Capacity/Specific Capacitance	Cycling Stability	Rate Capability	Energy Density $(Whkg^{-1})$	Power Density (Wkg^{-1})	Ref.
				$NiMoO_4$-metal hydroxide composite					
$NiMoO_4$-$Ni(OH)_2$	core	nanorod	-	7.43 Fcm^{-2} (4 $mAcm^{-2}$)	72% (1000 cycles)	3.06 Fcm^{-2} (112 $mAcm^{-2}$)	-	-	[113]
$NiMoO_4$-$Co(OH)_2$	core	nanowire	-	2.335 Fcm^{-2} (5 $mAcm^{-2}$)	83% (5000 cycles)	0.909 Fcm^{-2} (50 $mAcm^{-2}$)	-	-	[114]
Ni-Co LDH-$NiMoO_4$	shell	nanosheet	100.6	2100 Fg^{-1} (1 Ag^{-1})	91% (5000 cycles)	780 Fg^{-1} (10 Ag^{-1})	538.3	2522	[116]
$NiMoO_4$-Ni-Co LDH-$NiCo_2O_4$	shell	nanosheet	-	1035 Cg^{-1} (2587.5 Fg^{-1}) at 1 Ag^{-1}	80.6% (5000 cycles)	688 Cg^{-1} (20 Ag^{-1})	66.8	900	[117]
P-CoCH-$NiMoO_4$	core	nanosheet	-	5.08 Fcm^{-2} (2 $mAcm^{-2}$)	82.7% (2000 cycles)	3.27 Fcm^{-2} (20 $mAcm^{-2}$)	-	-	[118]
				$NiMoO_4$-metal chalcogenide composite					
$NiMoO_4$-Co_3S_4	core	nanosheet	62.04	359.31 $mAhg^{-1}$ (0.5 Ag^{-1})	82.9% (10000 cycles)	56.94 $mAhg^{-1}$ (10 Ag^{-1})	33.4	387.50	[121]
$NiMoO_4$-MoS_2	core	nanorod	58.8	2246.7 Fg^{-1} (1 Ag^{-1})	88.4% (5000 cycles)	1200.4 Fg^{-1} (20 Ag^{-1})	47.5	440	[122]
$NiMoO_4$-Ni_3S_2	core	nanorod	-	2.3 Fcm^{-2} (1 $mAcm^{-2}$)	84.4% (6000 cycles)	69.6% (40 $mAcm^{-2}$)	158.4 $mWhcm^{-2}$	2.199 Wcm^{-2}	[124]
Ni_3S_2-$NiMoO_4$	shell	nanosheet	-	1327.3 $\mu Ahcm^{-2}$ (2 $mAcm^{-2}$)	96.7% (6000 cycles)	900.9 $\mu Ahcm^{-2}$ (40 $mAcm^{-2}$)	121.5	2.285 $kW\ kg^{-1}$	[125]
$NiMoO_4$-NiS_2/MoS_2	core	nanowire	27.5	970 Fg^{-1} (5 Ag^{-1})	-	711 Fg^{-1} (20 Ag^{-1})	26.8	700	[126]
$NiMoO_4$-Ni_9S_8/MoS_2	core	nanorod	27.96	488.9 Fg^{-1} (1 Ag^{-1})	81% (10000 cycles)	52.9 Fg^{-1} (20 Ag^{-1})	-	-	[127]
$NiMoO_4$-C-Ni_3S_2	core	nanowire	-	7.9 Fcm^{-2} (5 $mAcm^{-2}$)	78.9% (3000 cycles)	1.57 Fcm^{-2} (50 $mAcm^{-2}$)	1.29 $mWhcm^{-3}$	13.99 Wcm^{-3}	[128]
$NiCo_2S_4$-$NiMoO_4 \cdot xH_2O$	shell	nanosheet	-	830.2 Fg^{-1} (2 Ag^{-1})	89.9% (5000 cycles)	380.9 Fg^{-1} (20 Ag^{-1})	19.3	795.7	[129]

Table 2. *Cont.*

Core-Shell Structure	Role of NiMoO$_4$	Morphology of NiMoO$_4$	Surface Area (m^{2}g^{-1})	Specific Capacity/Specific Capacitance	Cycling Stability	Rate Capability	Energy Density (Whkg^{-1})	Power Density (Wkg^{-1})	Ref.
NiCo$_2$S$_4$-NiMoO$_4$	shell	nanosheet	-	1487.6 Fg^{-1} (1 Ag^{-1})	89.7% (8000 cycles)	1154.3 Fg^{-1} (20 Ag^{-1})	53.2	560	[130]
NiCo$_2$S$_4$-NiMoO$_4$	shell	nanosheet	-	2006 Fg^{-1} (5 mAcm^{-2})	75% (2000 cycles)	1305 Fg^{-1} (50 mAcm^{-2})	21.4	58	[131]
NiCo$_2$S$_4$-NiMoO$_4$	shell	nanosheet	95	1714 Fg^{-1} (1 Ag^{-1})	96% (5000 cycles)	1314 Fg^{-1} (20 Ag^{-1})	29.1	172	[132]
NiCo$_2$S$_4$-NiMoO$_4$	shell	nanosheet	10.08	673.3 μAhcm^{-2} (5 mAcm^{-2})	84.2% (2000 cycles)	636.7 μAhcm^{-2} (100 mAcm^{-2})	33.1	219	[133]
NiCo$_2$O$_x$S$_y$-NiMoO$_4$	shell	nanosheet	-	17.75 Fcm^{-2} (1345 Fg^{-1}) at 10mAcm^{-2}	69.3% (2000 cycles)	43% (50 mAcm^{-2})	5.28	329	[134]
NiMoO$_4$-Ni-Co-S	core	nanorod	-	1892 Fg^{-1} (5 mAcm^{-2})	91.7% (6000 cycles)	842 Fg^{-1} (40 mAcm^{-2})	2.45 mWh cm^{-3}	0.131 Wcm^{-3}	[135]
NiMoO$_4$/CoMoO$_4$-Ni-Co-S	NiMoO$_4$/CoMoO$_4$ core	nanorod	-	778.1 Fg^{-1} (0.5 Ag^{-1})	98% (5000 cycles)	648.4 Fg^{-1} (4 Ag^{-1})	33.1	199.6	[123]
rGO-NiMoO$_4$-Ni-Co-S	core	NiMoO$_4$ hollow nanotube	-	318 mAhg^{-1} (1 Ag^{-1})	88.87% (10000 cycles)	212 mAhg^{-1} (20 Ag^{-1})	57.24	801.8	[136]
Ni-Co-Se-NiMoO$_4$	shell	nanosheet	114	396.1 mAhg^{-1} (1 Ag^{-1})	87.6% (8000 cycles)	283.3 mAhg^{-1} (20 Ag^{-1})	63.1	799.8	[137]
NiMoO$_4$-NiMoS$_4$	core	nanorod	18.6	832.3 Fg^{-1} (5 A g^{-1})	81.4% (1000 cycles)	555 Fg^{-1} (15 Ag^{-1})	22.84	3750	[138]
NiMoO$_4$-carbon material composite									
C-NiMoO$_4$	shell	nanograin	-	268.8 Fg^{-1} (0.5 Ag^{-1})	88.4% (2000 cycles)	168.4 Fg^{-1} (10 Ag^{-1})	-	-	[139]
Carbon nanofiber-NiMoO$_4$	shell	nanosheet	280	1840 Fg^{-1} (1 Ag^{-1})	78.3% (10000 cycles)	78% (20 Ag^{-1})	23.9	750	[140]
N-C-NiMoO$_4$	shell	nanosheet	258.2	1242 Fg^{-1} (1 Ag^{-1})	82.9% (2000 cycles)	581 Fg^{-1} (20 Ag^{-1})	44.6	250.4	[141]
XMoO$_4$-carbon submicrofiber (X = Ni, Co)	shell	nanosheet	75.722	1600 Fg^{-1} (1 Ag^{-1})	90.7% (3000 cycles)	1166 Fg^{-1} (10 Ag^{-1})	55.33	999.89	[142]

Table 2. *Cont.*

Core-Shell Structure	Role of NiMoO$_4$	Morphology of NiMoO$_4$	Surface Area (m^{2}g^{-1})	Specific Capacity/Specific Capacitance	Cycling Stability	Rate Capability	Energy Density (Whkg^{-1})	Power Density (Wkg^{-1})	Ref.
NiMoO$_4$-CNTs-CuO	shell	nanosheet	7.08	23.40 Fcm^{-2} (2 mAcm^{-2})	82.53% (10000 cycles)	12.9 Fcm^{-2} (22 mAcm^{-2})	96.40 mWhcm^{-3}	0.4 Wcm^{-3}	[143]
NiMoO$_4$/ V$_2$CT$_x$-rGO	NiMoO$_4$/ V$_2$CT$_x$ as yolk	nanoparticle	100.74	1022 Fg^{-1} (1 Ag^{-1})	88.9% (3000 cycles)	827 Fg^{-1} (10 Ag^{-1})	56.1	800	[144]
NiMoO$_4$-conductive polymer structures									
NiMoO$_4$-PANI	core	nanorod	56.14	1214 Fg^{-1} (1 Ag^{-1})	80.7% (2000 cycles)	813 Fg^{-1} (20 Ag^{-1})	33.07	240	[145]
PPy-NiMoO$_4$	core	nanowire	-	3.4 Fcm^{-2} (5 mAcm^{-2})	94% (5000 cycles)	2.30 Fcm^{-2} (50 mAcm^{-2})	0.5 mWcm^{-2}	3.7 mWhcm^{-2}	[146]
NiCo$_2$O$_4$-NiMoO$_4$/PANI	shell	nanoplate	-	2.38 Fcm^{-2} (1 mAcm^{-2})	92.36% (5000 cycles)	1.508 Fcm^{-2} (10 mAcm^{-2})	90	443.2	[147]
NiO-NiMoO$_4$-PPy	NiMoO$_4$ and PPy as shell	porous spherical nanostructure	170.10	1645.1 Fg^{-1} (1 Ag^{-1})	77.1% (30000 cycles)	843.2 Fg^{-1} (20 Ag^{-1})	-	-	[148]

4.4. NiMoO$_4$-Carbon Material Composite

Carbon materials such as porous carbon, activated carbon, carbon fiber, carbon nanotube, and graphene are often exploited as supercapacitor materials. They have a high active surface area, excellent electrical conductivity, good chemical stability, and robust mechanical strength. Nevertheless, their practical applications are limited because the specific capacitance is less compared to transition metal oxides. Combining carbon materials with NiMoO$_4$ can significantly improve cycling stability and rate capability. The grouping can take complete benefits of superior electrical conductivity, great SSA from carbon materials, and high specific capacitance from NiMoO$_4$.

The hierarchical C-NiMoO$_4$ composite was synthesized via a two-step hydrothermal method [139]. The NiMoO$_4$ nanograins were strongly attached to the surface of carbon spheres (CSs), creating a rough silkworm-cocoon-like composite material. The unique structured electrode exhibited good performance due to the following features: (i) highly conductive CSs considerably decrease the charge transfer resistance of the electrode, (ii) the strong bonding between NiMoO$_4$ and CSs leads to improved electron/ion diffusion, (iii) the exclusive structure has excellent mechanical adhesion, therefore, improving the electrode stability. The specific capacitance (C$_{sp}$) was maximum up to 268.8 Fg^{-1} at 0.5 Ag^{-1} and the value reduced to 168.4 Fg^{-1} at 10 Ag^{-1} because of the inadequate interaction between the electrode and electrolyte ions. The coaxial carbon-NiMoO$_4$ composite nanofibers were reported for the supercapacitor electrode [140]. The uniform NiMoO$_4$ nanosheets were deposited on electrospun carbon nanofibers (CNFs) via a microwave-assisted hydrothermal method followed by a thermal process. The rough surface of conductive CNFs (diameter~400 nm) offers abundant nucleation sites for the growth of the NiMoO$_4$ shell layer, which is made up of numerous nanosheets, as evident from TEM analysis. The thickness of the mesoporous NiMoO$_4$ layer can be tuned by varying the concentration of the precursor solution. The nanosheets create intimate contact with the CNFs, which favors the electron transfer and increases the redox active surface (SSA~280 m^{2}g^{-1}). Also, the high porosity of CNFs enables the infiltration of electrolytes into the composite, which is essential for high-rate capability. Due to these benefits, the specific capacitance reached 1840 Fg^{-1} at 1 Ag^{-1} with 78.3% capacity retention (10,000 cycles). N-C-NiMoO$_4$ double-shelled hollow microtubes were developed from nitrogen-doped carbon (N-C) nanotubes (inner shell) and NiMoO$_4$ nanosheets (outer shell) [141]. Initially, PPy nanotubes were converted into N-C nanotubes by calcining in an argon atmosphere. Next, a SiO$_2$ layer was applied to the N-C nanotube surface. Finally, NiMoO$_4$ nanosheets were in-situ grown on the N-C nanotube surface through a hydrothermal process, after which the N-C-NiMoO$_4$ composite was attained by eliminating residual SiO$_2$ via calcination and etching processes. The N-C nanotubes prevent NiMoO$_4$ nanosheets from stacking and aggregation, which ultimately leads to a hollow tube structure with high SSA (258.2 m^{2}g^{-1}, average pore size~9.164 nm) and creates NiMoO$_4$ nanosheets with increased active sites. At 1 Ag^{-1}, the specific capacitance attained a maximum of 1242 Fg^{-1}.

NiMoO$_4$-CMFs (carbon submicrofibers), CoMoO$_4$-CMFs, and NiMoO$_4$-HPCMFs (hollow porous carbon submicrofibers) were constructed via electrospinning followed by the hydrothermal method [142]. The SEM images of NiMoO$_4$-CMFs and NiMoO$_4$-HPCMFs are shown in Figure 8a,c. At 1 Ag^{-1}, NiMoO$_4$-CMFs delivered a higher specific capacitance and cycling stability (1485.53 Fg^{-1}, 87.6% after 3000 cycles) compared to CoMoO$_4$-CMFs (1407.1 Fg^{-1}, 80.6% after 3000 cycles). The growth of thin NiMoO$_4$ nanosheets (ca. 250 nm) over CMFs and HPCMFs was confirmed by TEM images (Figure 8b,d). Benefiting from the hollow and mesoporous structure with a pore size of ca. 3 nm (Figure 8e), HPCMFs can offer large SSA for electrolyte infiltration and provide additional channels for electron/ion transport. At 1 Ag^{-1}, the specific capacitance of NiMoO$_4$-HPCMFs was 1600 Fg^{-1}, and cycling stability was 90.7% after 3000 cycles. Novel NiMoO$_4$ NSs-CNTs-CuO nanowire arrays (NWAs) were rationally constructed on Cu foam using electrodeposition and hydrothermal methods by Yao et al. [143]. Carbon nanotubes (CNTs) strongly wrapped over Cu(OH)$_2$ nanowires supported on Cu skeleton to form conductive network channels, contributing

to the rapid electron/ion diffusion. CNTs-Cu(OH)$_2$ NWAs were enclosed by NiMoO$_4$ nanosheets (NSs) to create core-shell nanowires. After calcination, the resulting highly porous NiMoO$_4$ NSs-CNTs-CuO NWAs demonstrate a large surface area with abundant active sites for redox reactions, which can improve energy storage. At 2 mAcm^{-2}, the supercapacitor electrode exhibited an ultrahigh areal specific capacitance of 23.4 Fcm^{-2}. Chen et al. [144] constructed a hollow NiMoO$_4$/V$_2$CT$_x$-rGO yolk-shell composite employing a novel room temperature ionic liquid (RTIL)-assisted hydrothermal method, as illustrated in Figure 8f. First, NiMoO$_4$ was incorporated into the V$_2$CT$_x$ MXene layer in the presence of RTIL, named 1-butyl-3-methylimidazole tetrafluoroborate ([Bmim]BF$_4$). Then, rGO was applied to the NiMoO$_4$/V$_2$CT$_x$ yolk under electrostatic forces. The [Bmim]BF$_4$ avoids over-oxidation of V$_2$CT$_x$ MXene during the preparation of NiMoO$_4$ and decreases its surface energy, which makes the NiMoO$_4$/V$_2$CT$_x$-rGO composite with high stability. In Figure 8g,h, the TEM images of NiMoO$_4$/V$_2$CT$_x$-rGO confirmed the formation of a yolk-shell structure with a definite void space between the inner core and the outer shell. HRTEM images revealed the uniform distribution of MXene sheets, which further confirmed that NiMoO$_4$ nanoparticles did not leave the MXene sheet to create large clusters due to the magnetic properties (Figure 8i,j). As shown in Figure 8k, the CV curves are similar in shape, and a pair of redox peaks represent pseudocapacitive behavior. After 3000 cycles, the electrode retained 88.9% of its initial capacity, specifying good cycling stability (Figure 8l). At 1 Ag^{-1}, the specific capacitance was 1022 Fg^{-1}, which can be assigned to the following reasons. (1) The yolk-shell structure with large SSA and porosity significantly improves ion diffusion, (2) The petal-folded NiMoO$_4$ nanoparticles are dispersed over the surface or layered structure of V$_2$CT$_x$, resulting in abundant active sites; meanwhile, aggregation of rGO is impeded, (3) The rGO shell develops conductive channels for electrons. Also, a bamboo-shaped MoO$_2$-Fe$_2$O$_3$/NC (N-doped carbon) anode was designed on CC using electrochemical deposition. The NiMoO$_4$/V$_2$CT$_x$-rGO//MoO$_2$-Fe$_2$O$_3$/NC device attained a high energy-density of 56.1 Whkg^{-1} at a power density of 800 Wkg^{-1}. Wang et al. [149] hydrothermally developed the 2D/2D NiMoO$_4$/MXene nanosheets with an interconnected porous network. The hydrophilic properties of Ti$_3$C$_2$T$_x$ and its superior electrical conductivity, as well as the synergistic interactions between NiMoO$_4$ and Ti$_3$C$_2$T$_x$, all contributed to the high specific capacity of 545.5 Cg^{-1} at 0.5 Ag^{-1}.

4.5. NiMoO$_4$-Conductive Polymer Composite

Conductive polymers of polyaniline (PANI) and polypyrrole (PPy) exhibit interesting features of high electrical conductivity, fast reversible Faradaic reactions, high charge density, and high flexibility [145]. Meanwhile, low SSA, limited charge/discharge cycles, and difficult processing hinder their practical applications. Therefore, these materials can be grouped with NiMoO$_4$ to improve electrochemical performance. Highly-conductive NiMoO$_4$-PANI nanocomposite was synthesized via solvothermal followed by chemical polymerization [145]. The surface of mesoporous NiMoO$_4$ nanorods is uniformly covered by PANI, which could effectively reduce the pore size (~7.8 nm) and prevent the aggregation of nanorods as well as afford active sites for electron/ion diffusion. At 1 Ag^{-1}, the specific capacitance reached 1214 Fg^{-1}. After 2000 cycles, the cycling stability was 80.7% at 5 Ag^{-1}. The 3D PPy/NiMoO$_4$/CC heterostructure was developed by adopting hydrothermal and chemical polymerization methods [146]. NiMoO$_4$ and PPy/NiMoO$_4$ were evenly distributed on CC (Figure 9a,c). The smooth surface of NiMoO$_4$ nanowires became rough due to the introduction of PPy, and the diameter of the nanowire reasonably increased, as depicted in Figure 9b,d. As shown in Figure 9e, PPy/NiMoO$_4$/CC displayed a better areal-specific capacitance of 3.4 Fcm^{-2} at 5 mAcm^{-2} compared to NiMoO$_4$/CC due to the decrease of ion diffusion length and charge transfer impedance. The exterior bulge-like PPy nanostructure could overcome the volume change and improve material utilization during the charge/discharge process, contributing to excellent cycling stability of 94% over 5000 cycles (Figure 9f). The PPy/NiMoO$_4$//AC device provided an energy density of

0.5 mWcm^{-2} at a power density of 3.7 mWhcm^{-2} and exhibited good flexibility without any obvious change in the CV curves under different deformation conditions.
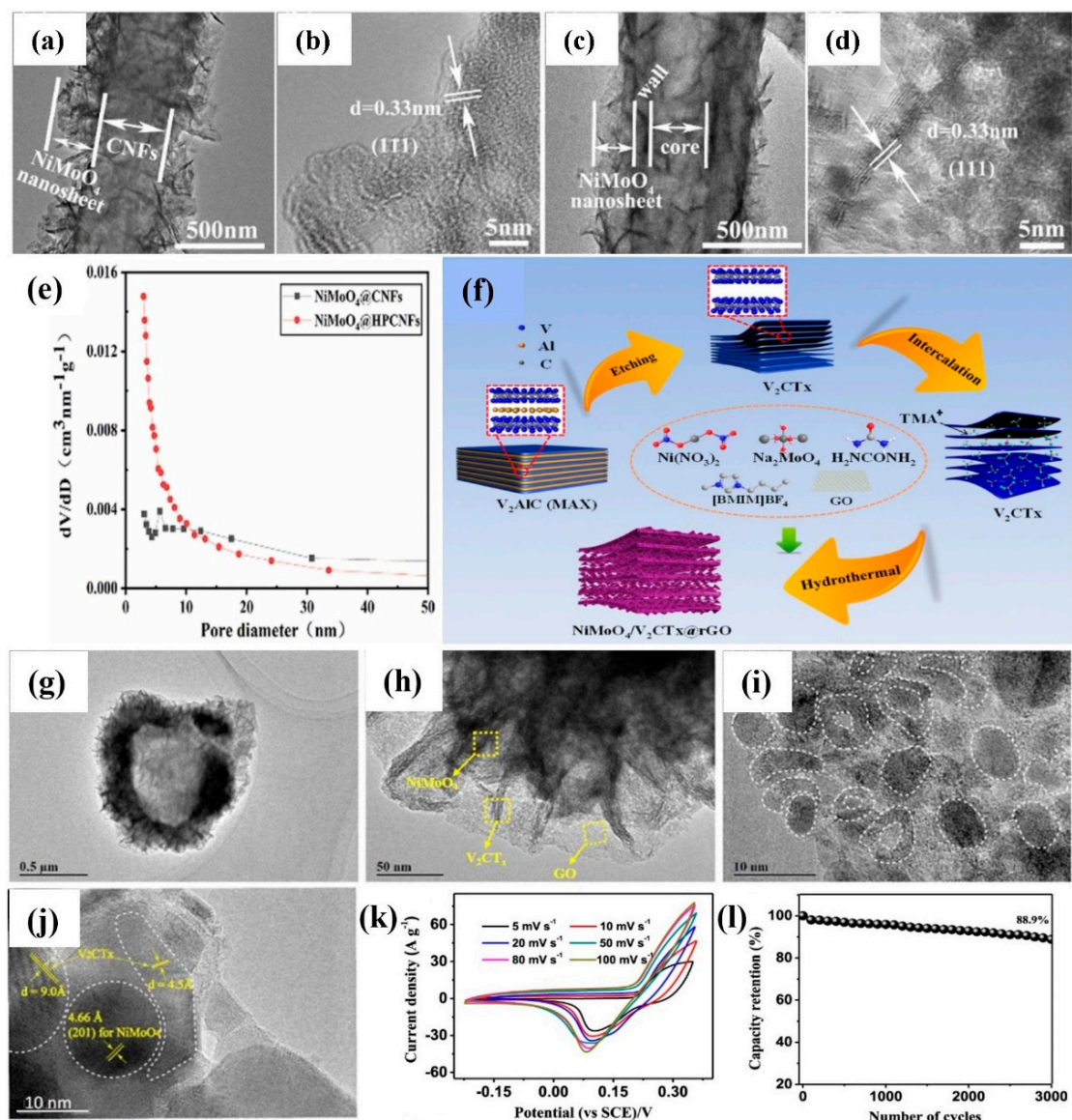

Figure 8. (**a**,**c**) SEM images of NiMoO$_4$−CMFs and NiMoO$_4$−HPCMFs, (**b**,**d**) TEM images of NiMoO$_4$−CMFs and NiMoO$_4$−HPCMFs, (**e**) Pore diameter distribution [142]. Reproduced from Ref. [142] with permission from Elsevier, 2022. (**f**) Schematic diagram of the formation of NiMoO$_4$/V$_2$CT$_x$−rGO MXene, (**g**,**h**) TEM images of NiMoO$_4$/V$_2$CT$_x$−rGO, (**i**,**j**) HRTEM images of NiMoO$_4$/V$_2$CT$_x$−rGO, (**k**) CV curves at various scan rates, (**l**) Cycling stability at 10 Ag^{-1} [144]. Reproduced from Ref. [144] with permission from American Chemical Society, 2021.

Shen and co-workers [147] demonstrated holothurian-like NiCo$_2$O$_4$-NiMoO$_4$/PANI nanocomposites. NiCo$_2$O$_4$ nanowires and NiMoO$_4$ nanoplates were hydrothermally grown on CC, and then highly conductive 3D PANI nanorods were deposited on the surface of NiCo$_2$O$_4$-NiMoO$_4$ nanoflowers by in-situ polymerization. At 1 mAcm^{-2}, the areal specific capacitance reached a maximum of 2.38 Fcm^{-2}, and cycling stability was 92.36% after 5000 cycles. This is because the holothurian-like morphology significantly improves the surface area and reduces the charge transfer distance. Additionally, the active channels in NiCo$_2$O$_4$-NiMoO$_4$/PANI structure and polar groups on PANI can facilitate ion diffusion, resulting in high ionic conductivity. A spherical NiO-NiMoO$_4$-PPy nanostructure was constructed along with NiO, NiMoO$_4$, and NiO-NiMoO$_4$ [148]. Only NiO shows

flower-like morphology, and all other nanostructures of $NiMoO_4$, NiO-$NiMoO_4$, and NiO-$NiMoO_4$-PPy exhibit porous structures composed of interconnected nanosheets. The SSA of NiO-$NiMoO_4$-PPy (170.10 m^2g^{-1}) is lower than that of NiO-$NiMoO_4$ (258.78 m^2g^{-1}) because PPy occupies the interspace. The introduction of $NiMoO_4$ and PPy shell structures can efficiently reduce the charge transfer resistance and increase the redox reaction by providing high electrical conductivity; meanwhile, the PPy also offers additional mechanical strength to the nanostructure. All CV curves are similar in shape with the increasing scan rate, indicating the pseudocapacitive behavior of NiO-$NiMoO_4$-PPy. Figure 9g illustrates that GCD curves exhibit nearly symmetric, nonlinear triangular shapes and steady discharge plateaus at different current densities (1–20 Ag^{-1}). Specifically, NiO-$NiMoO_4$-PPy displays the longest discharge times at each current density, signifying the largest specific capacitance (Figure 9h). At 1 Ag^{-1}, the specific capacitance attained a maximum of 1645.1 Fg^{-1}, and it was reduced to 843.2 Fg^{-1} at 20 Ag^{-1}, showing its exceptional rate capability. The capacity retention was 77.1% after 30,000 cycles (Figure 9i). From density functional theory (DFT) calculations, it was suggested that much stronger Mo-O bonding is crucial to stabilize NiO-$NiMoO_4$ nanostructure, which would result in good cycling stability.
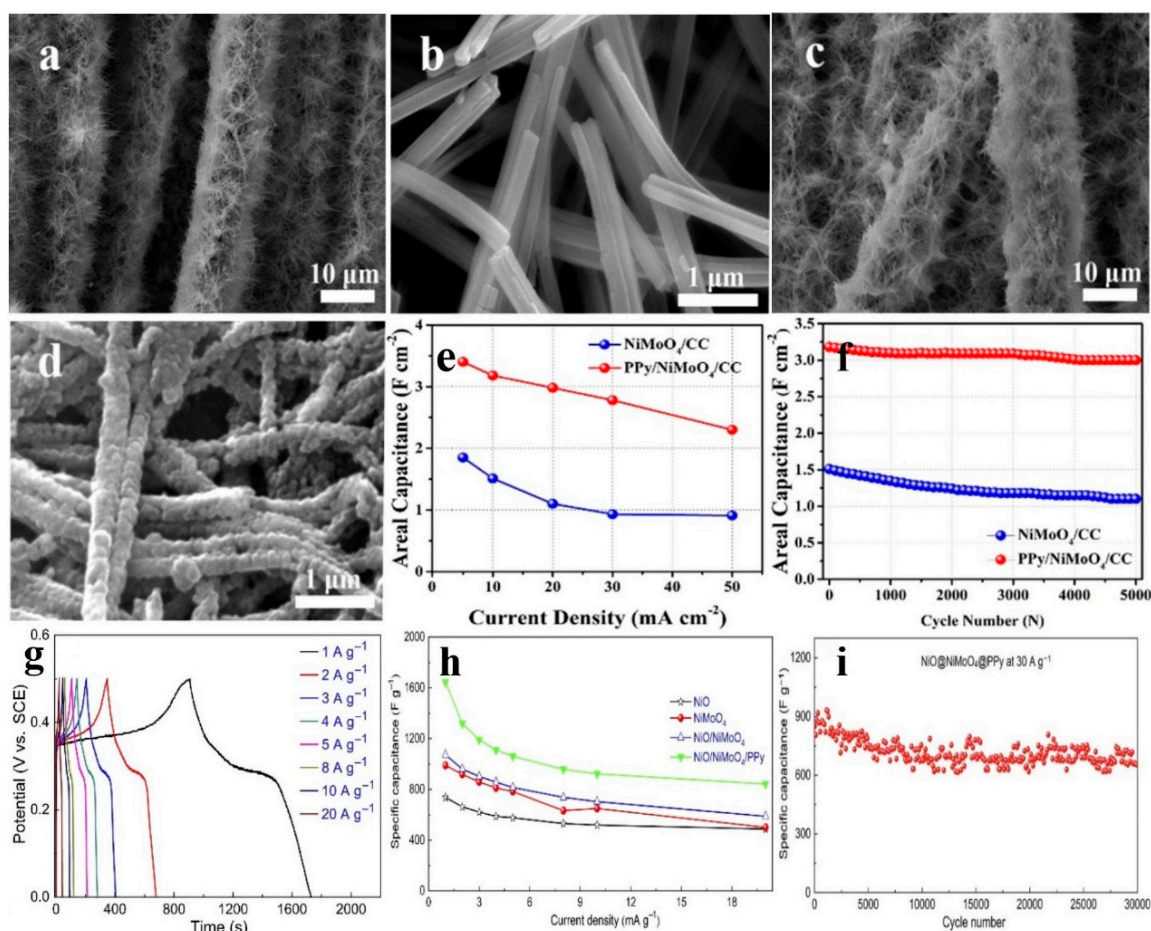

Figure 9. SEM images of the $NiMoO_4$/CC and $PPy/NiMoO_4$/CC electrodes: (**a**,**c**) low−magnification, (**b**,**d**) high−magnification, (**e**) specific capacitance at various current densities, and (**f**) cycling performance at a discharge rate of 10 $mAcm^{-2}$ [146]. Reproduced from Ref. [146] with permission from Elsevier, 2020. (**g**) GCD curves of NiO−$NiMoO_4$−PPy at different current densities (1–20 Ag^{-1}), (**h**) Specific capacitances of NiO, $NiMoO_4$, NiO−$NiMoO_4$ and NiO−$NiMoO_4$−PPy calculated by GCD curves, (**i**) Long−term cycling stability of NiO−$NiMoO_4$−PPy at 30 Ag^{-1} [148]. Reproduced from Ref. [148] with permission from Elsevier, 2020.

5. Conclusions

SCs (or ECs) have great potential in the field of energy storage devices. Fabricating the electrode material in a core-shell structure can be one of the effective ways to improve the SCs overall performance. The use of the carefully chosen composite material for the core-shell structure can also benefit from synergistic material effects for better SCs performance. The excellent electrode characteristics would stem from their inherent properties, such as unique morphology and/or porous structure, good electrical conductivity, high redox activity, and good stability.

$NiMoO_4$, a promising pseudocapacitive material, has been used to form a composite material with additional materials, including metal oxides, metal hydroxides, metal chalcogenides, carbon, and conductive polymers. These composite materials could be fabricated into the core-shell nanostructures to boost the electrochemical performance for SCs application. This paper reviewed those core-shell structures in detail and summarized them in terms of methodological aspects and their relevant properties for SCs applications.

6. Future Perspectives

We provide several points which can lend themselves to the future research focus to improve the performance of the hybrid core-shell structure using the $NiMoO_4$-based composite materials for SCs application as follows:

1. The porous structure of the core-shell-based devices possesses the advantages of the enhancement of the electrode-electrolyte contact area and the shortened distance of electron/ion diffusion from the active medium to the current collector. The morphological feature of the porous core-shell structure is nearly independent of the choice of substrate used to grow the $NiMoO_4$ composite through the hydrothermal method. Those advantages can lead to superior specific capacitance rate capability and long cycling stability. However, its poor crystallinity that possibly occurs may pose the challenge of inadequate electrical conductivity. This possible shortcoming can be compensated for by the use of the proper substrate. Additional focus can be placed on the substrate for optimizing the SCs' performances;

2. When compared with other synthesis methods, the hydrothermal approach offers a direct and efficient way to synthesize distinctive core-shell composites based on $NiMoO_4$ and to get improved electrochemical performances by modifying the temperature, reaction time, type, and concentration of surfactants. This method plays a crucial role in the morphology of the composite material. For example, when the reaction time exceeds that required, the shell thickness becomes increased and disordered, with the consequence of distorting/collapsing the original structure and eventually producing cracks. This would, in turn, result in poor electrolyte infiltration. Moreover, mass loading should be optimized as it affects the specific capacitance and energy storage capacity. Future research needs to focus on such parameter optimization for better SCs performance;

3. The choice of electrolyte based on conductivity and ionic mobility is crucial for good supercapacitive performance. Generally, aqueous electrolytes have higher conductivity than non-aqueous and solid electrolytes due to their low dynamic viscosity. Aqueous electrolytes, such as alkali metal-based hydroxy (KOH, NaOH) and sulfate electrolytes (Na_2SO_4, H_2SO_4), are commonly used for supercapacitors. The KOH electrolyte is the most popular among all due to its smaller hydrated ions (ionic radius~3.31 Å), therefore often used in all types of the core-shell structures of the $NiMoO_4$-based composites;

4. Various morphologies for the core-shell structures of the $NiMoO_4$-based composite materials have been investigated, such as the nanosheets, the nanowires, the nanorods, and the nanoflakes. Among those reported, the nanosheets exhibited a higher specific capacitance than the others due to a large SSA. They could also facilitate fast electron/ion transport with increasing conductive channels and hold up their volume

during the long charge/discharge cycles. These merits can lead nanosheets to gather more research interests for finding SCs applications;

5. The combination of Ni-Co-based oxides with $NiMoO_4$ has often been reported in the literature. When compared to all other core-shell composites, Ni-Co-based sulfides coupled with $NiMoO_4$ for the core-shell structures showed superior electrochemical performance due to the participation of Ni^{2+}/Ni^{3+} and Co^{2+}/Co^{3+} in redox reactions. Moreover, cobalt sulfides, as opposed to their oxide counterparts, have a more varied crystal structure, high electrical conductivity, and good electrochemical activity;

6. To date, only a few reports are available on $NiMoO_4$-based core-shell composites consisting of metal sulfides, carbon materials, and conductive polymers. Therefore, other types of mixed transition metal oxides (metal tungstates, metal vanadates)/sulfides can be exploited with $NiMoO_4$ for core-shell composites to achieve a higher reversible redox activity and specific capacitance than the single metal oxides/sulfides;

7. Compact and flexible energy storage devices can be developed for advanced thin and wearable electronics. The complex, hollow, and branched core-shell nanostructured composites can be designed to fit the future supercapacitor.

Author Contributions: Conceptualization, H.J.; methodology, K.S.; software, K.S.; validation, K.S. and H.J.; formal analysis, K.S. and H.J.; investigation, K.S. and H.J.; resources, H.J.; data curation, K.S. and H.J.; writing—original draft preparation, K.S. and H.J.; writing—review, H.J.; visualization, K.S. and H.J.; supervision, H.J.; project administration, H.J.; funding acquisition, H.J. All authors have read and agreed to the published version of the manuscript.

Institutional Review Board Statement: Not applicable.

Informed Consent Statement: Not applicable.

Data Availability Statement: The data presented in this study are available on request from the corresponding author. The data are not publicly available due to privacy.

Conflicts of Interest: The authors declare that they have no known competing financial interests or personal relationships that could have appeared to influence the work reported in this paper.

Abbreviations

1D—One-dimensional; 2D—Two-dimensional; 3D—Three-dimensional; AC—Activated carbon; ASC—Asymmetric supercapacitor; BET—Brunauer-Emmett-Teller analysis; CC—Carbon cloth; CNT—Carbon nanotube; CS—Carbon sphere; DFT—Density functional theory; EDS—Energy-dispersive X-ray spectroscopy; EDLC—Electrochemical double-layer capacitor; EIS—Electrochemical impedance spectroscopy; GCD—Galvanostatic charge/discharge; GO—Graphene oxide; HSC—Hybrid supercapacitor; HRTEM—High-resolution transmission electron microscope; LDH—Layered double hydroxide; MOF—Metal-organic framework; NCMO—$NiMoO_4$/$CoMoO_4$; NCMOS—$NiMoO_4$/$CoMoO_4$-NiCoS; NF—Nickel foam; PANI—Polyaniline; PC—Pseudo capacitor; PPy—Polypyrrole; PVA—Polyvinyl alcohol; rGO—Reduced graphene oxide; SC—Supercapacitor; SAED—Selected area electron diffraction; SEM—Scanning electron microscopy; SSA—Specific surface area; SSC—Symmetric supercapacitor; TEM—Transmission electron microscopy.

References

1. Singh, S.; Jain, S.; Venkateswaran, P.S.; Tiwari, A.K.; Nouni, M.R.; Pandey, J.K.; Goel, S. Hydrogen: A sustainable fuel for future of the transport sector. *Renew. Sustain. Energy Rev.* **2015**, *51*, 623–633. [CrossRef]
2. Liu, X.; Chen, S.; Xiong, Z.; Li, K.; Zhang, Y. Tungsten oxide-based nanomaterials for supercapacitors: Mechanism, fabrication, characterization, multifunctionality, and electrochemical performance. *Prog. Mater. Sci.* **2022**, *130*, 100978. [CrossRef]
3. Huang, S.; Zhu, X.; Sarkar, S.; Zhao, Y. Challenges and opportunities for supercapacitors. *APL Mater.* **2019**, *7*, 100901. [CrossRef]
4. Swain, N.; Saravanakumar, B.; Kundu, M.; Schmidt-Mende, L.; Ramadoss, A. Recent trends in template assisted 3D porous materials for electrochemical supercapacitors. *J. Mater. Chem. A* **2021**, *9*, 25286–25324. [CrossRef]

5.	Borenstein, A.; Hanna, O.; Attias, R.; Luski, S.; Brousse, T.; Aurbach, D. Carbon-based composite materials for supercapacitor electrodes: A review. *J. Mater. Chem. A* **2017**, *5*, 12653–12672. [CrossRef]

6.	Sun, J.; Huang, Y.; Sea, Y.N.S.; Xue, Q.; Wang, Z.; Zhu, M.; Li, H.; Tao, X.; Zhi, C.; Hu, H. Recent progress of fiber-shaped asymmetric supercapacitors. *Mater. Today Energy* **2017**, *5*, 1–14. [CrossRef]

7.	Kour, S.; Tanwar, S.; Sharma, A. A review on challenges to remedies of MnO_2 based transition-metal oxide, hydroxide, and layered double hydroxide composites for supercapacitor applications. *Mater. Today Commun.* **2022**, *32*, 104033. [CrossRef]

8.	Low, W.H.; Khiew, P.S.; Lim, S.S.; Siong, C.W.; Ezeigwe, E.R. Recent development of mixed transition metal oxide and graphene/mixed transition metal oxide based hybrid nanostructures for advanced supercapacitors. *J. Alloys Compd.* **2018**, *775*, 1324–1356. [CrossRef]

9.	Francis, M.K.; Bhargav, P.B.; Ramesh, A.; Ahmed, N.; Balaji, C. Electrochemical performance analysis of $NiMoO_4/\alpha\text{-}MoO_3$ composite as anode material for high capacity lithium-ion batteries. *Appl. Phys. A* **2022**, *128*, 132. [CrossRef]

10.	Deng, W.; Ji, X.; Chen, Q.; Banks, C.E. Electrochemical capacitors utilising transition metal oxides: An update of recent developments. *RSC Adv.* **2011**, *1*, 1171–1178. [CrossRef]

11.	Maksoud, M.I.A.A.; Reheem, A.M.A.; Waly, S.A.; Fahim, R.A.; Ahour, A.H. Tuning the structure, optical, and magnetic properties of nanostructured $NiMoO_4$ by nitrogen plasma treatment. *Appl. Phys. A* **2022**, *128*, 300. [CrossRef]

12.	Ray, S.K.; Joshi, B.; Ramani, S.; Park, S.; Hur, J. Multicolor and white light upconversion luminescence in $\alpha\text{-}NiMoO_4$:Yb^{3+}/Ln^{3+} (Ln = Tm, Ho, Tm/Ho) nanoparticles. *J. Alloys Compd.* **2021**, *892*, 162101. [CrossRef]

13.	Yang, L.; Wang, J.; Wan, Y.; Li, Y.; Xie, H.; Cheng, H.; Seo, H.J. Structure and effective visible-light-driven photocatalytic activity of $\alpha\text{-}NiMoO_4$ for degradation of methylene blue dye. *J. Alloys Compd.* **2015**, *664*, 756–763. [CrossRef]

14.	Jeseentharani, V.; Dayalan, A.; Nagaraja, K. Nanocrystalline composites of transition metal molybdate ($Ni_{1-x}Co_xMoO_4$; x = 0, 0.3, 0.5, 0.7, 1) synthesized by a co-precipitation method as humidity sensors and their photoluminescence properties. *J. Phys. Chem. Solids* **2018**, *115*, 75–83. [CrossRef]

15.	Zhang, Y.; Gao, H.-L.; Jia, X.-D.; Wang, S.-W.; Yan, J.; Luo, H.-W.; Gao, K.-Z.; Fang, H.; Zhang, A.-Q.; Wang, L.-Z. $NiMoO_4$ nanorods supported on nickel foam for high-performance supercapacitor electrode materials. *J. Renew. Sustain. Energy* **2018**, *10*, 054101. [CrossRef]

16.	Murugan, E.; Govindaraju, S.; Santhoshkumar, S. Hydrothermal synthesis, characterization and electrochemical behavior of $NiMoO_4$ nanoflower and $NiMoO_4$/rGO nanocomposite for high-performance supercapacitors. *Electrochim. Acta* **2021**, *392*, 138973. [CrossRef]

17.	Seevakan, K.; Manikandan, A.; Devendran, P.; Shameem, A.; Alagesan, T. Microwave combustion synthesis, magneto-optical and electrochemical properties of $NiMoO_4$ nanoparticles for supercapacitor application. *Ceram. Int.* **2018**, *44*, 13879–13887. [CrossRef]

18.	Moosavifard, S.E.; Shamsi, J.; Ayazpour, M. 2D high-ordered nanoporous $NiMoO_4$ for high-performance supercapacitors. *Ceram. Int.* **2015**, *41*, 1831–1837. [CrossRef]

19.	Jiang, L.-B.; Yuan, X.-Z.; Liang, J.; Zhang, J.; Wang, H.; Zeng, G.-M. Nanostructured core-shell electrode materials for electrochemical capacitors. *J. Power Sources* **2016**, *331*, 408–425. [CrossRef]

20.	Peng, S.; Li, L.; Bin Wu, H.; Madhavi, S.; Lou, X.W. Controlled growth of $NiMoO_4$ nanosheet and nanorod arrays on various conductive substrates as advanced electrodes for asymmetric supercapacitors. *Adv. Energy Mater.* **2014**, *5*, 1401172. [CrossRef]

21.	Minakshi, M.; Watcharatharapong, T.; Chakraborty, S.; Ahuja, R. A combined theoretical and experimental approach of a new ternary metal oxide in molybdate composite for hybrid energy storage capacitors. *APL Mater.* **2018**, *6*, 047701. [CrossRef]

22.	Eda, K.; Kato, Y.; Ohshiro, Y.; Sugitani, T.; Whittingham, M.S. Synthesis, crystal structure, and structural conversion of Ni molybdate hydrate $NiMoO_4 \cdot nH_2O$. *J. Solid State Chem.* **2010**, *183*, 1334–1339. [CrossRef]

23.	Rodriguez, J.A.; Hanson, J.C.; Chaturvedi, S.; Maiti, A.; Brito, J.L. Phase transformations and electronic properties in mixed-metal oxides: Experimental and theoretical studies on the behavior of $NiMoO_4$ and $MgMoO_4$. *J. Chem. Phys.* **2000**, *112*, 935–945. [CrossRef]

24.	Cao, Z.; Liu, C.; Huang, Y.; Gao, Y.; Wang, Y.; Li, Z.; Yan, Y.; Zhang, M. Oxygen-vacancy-rich $NiCo_2O_4$ nanoneedles electrode with poor crystallinity for high energy density all-solid-state symmetric supercapacitors. *J. Power Sources* **2020**, *449*, 227571. [CrossRef]

25.	Padmanathan, N.; Shao, H.; Razeeb, K.M. Honeycomb micro/nano-architecture of stable $\beta\text{-}NiMoO_4$ electrode/catalyst for sustainable energy storage and conversion devices. *Int. J. Hydrogen Energy* **2020**, *45*, 30911–30923. [CrossRef]

26.	Ma, X.-J.; Zhang, W.-B.; Kong, L.-B.; Luo, Y.-C.; Kang, L. $NiMoO_4$-modified MnO_2 hybrid nanostructures on nickel foam: Electrochemical performance and supercapacitor applications. *New J. Chem.* **2015**, *39*, 6207–6215. [CrossRef]

27.	Sharma, P.; Minakshi, M.; Whale, J.; Jean-Fulcrand, A.; Garnweitner, G. Effect of the Anionic Counterpart: Molybdate vs. Tungstate in Energy Storage for Pseudo-Capacitor Applications. *Nanomaterials* **2021**, *11*, 580. [CrossRef] [PubMed]

28.	Hussain, S.; Javed, M.S.; Asim, S.; Shaheen, A.; Khan, A.J.; Abbas, Y.; Ullah, N.; Iqbal, A.; Wang, M.; Qiao, G.; et al. Novel gravel-like $NiMoO_4$ nanoparticles on carbon cloth for outstanding supercapacitor applications. *Ceram. Int.* **2020**, *46*, 6406–6412. [CrossRef]

29.	Zhang, S.-W.; Yin, B.-S.; Liu, C.; Wang, Z.-B.; Gu, D.-M. $NiMoO_4$ nanowire arrays and carbon nanotubes film as advanced electrodes for high-performance supercapacitor. *Appl. Surf. Sci.* **2018**, *458*, 478–488. [CrossRef]

30.	Hao, Y.; Huang, H.; Wang, Q.; Wang, Q.; Zhou, G. Nitrogen-doped carbon/$NiMoO_4$ nanospheres assembled by nanosheets and ultrasmall nanoparticles for supercapacitors. *Chem. Phys. Lett.* **2019**, *728*, 215–223. [CrossRef]

31. Lin, L.; Liu, T.; Liu, J.; Sun, R.; Hao, J.; Ji, K.; Wang, Z. Facile synthesis of groove-like NiMoO$_4$ hollow nanorods for high-performance supercapacitors. *Appl. Surf. Sci.* **2016**, *360*, 234–239. [CrossRef]

32. Raj, C.J.; Manikandan, R.; Yu, K.H.; Nagaraju, G.; Park, M.-S.; Kim, D.-W.; Park, S.Y.; Kim, B.C. Engineering thermally activated NiMoO$_4$ nanoflowers and biowaste derived activated carbon-based electrodes for high-performance supercapatteries. *Inorg. Chem. Front.* **2020**, *7*, 369–384. [CrossRef]

33. Qing, C.; Yang, C.; Chen, M.; Li, W.; Wang, S.; Tang, Y. Design of oxygen-deficient NiMoO$_4$ nanoflake and nanorod arrays with enhanced supercapacitive performance. *Chem. Eng. J.* **2018**, *354*, 182–190. [CrossRef]

34. Cai, D.; Wang, D.; Liu, B.; Wang, Y.; Liu, Y.; Wang, L.; Li, H.; Huang, H.; Li, Q.; Wang, T. Comparison of the electrochemical performance of NiMoO$_4$ nanorods and hierarchical nanospheres for supercapacitor applications. *ACS Appl. Mater. Interfaces* **2013**, *5*, 12905–12910. [CrossRef]

35. Abbas, Y.; Yun, S.; Javed, M.S.; Chen, J.; Tahir, M.F.; Wang, Z.; Yang, C.; Arshad, A.; Hussain, S. Anchoring 2D NiMoO$_4$ nano-plates on flexible carbon cloth as a binder-free electrode for efficient energy storage devices. *Ceram. Int.* **2020**, *46*, 4470–4476. [CrossRef]

36. Cai, D.; Liu, B.; Wang, D.; Liu, Y.; Wang, L.; Li, H.; Wang, Y.; Wang, C.; Li, Q.; Wang, T. Enhanced performance of supercapacitors with ultrathin mesoporous NiMoO$_4$ nanosheets. *Electrochim. Acta* **2014**, *125*, 294–301. [CrossRef]

37. Chen, C.; He, S.; Dastafkan, K.; Zou, Z.; Wang, Q.; Zhao, C. Sea urchin-like NiMoO$_4$ nanorod arrays as highly efficient bifunctional catalysts for electrocatalytic/photovoltage-driven urea electrolysis. *Chin. J. Catal.* **2022**, *43*, 1267–1276. [CrossRef]

38. Cai, D.; Liu, B.; Wang, D.; Liu, Y.; Wang, L.; Li, H.; Wang, Y.; Wang, C.; Li, Q.; Wang, T. Facile hydrothermal synthesis of hierarchical ultrathin mesoporous NiMoO$_4$ nanosheets for high performance supercapacitors. *Electrochim. Acta* **2014**, *115*, 358–363. [CrossRef]

39. Huang, L.; Xiang, J.; Zhang, W.; Chen, C.; Xu, H.; Huang, Y. 3D interconnected porous NiMoO$_4$ nanoplate arrays on Ni foam as high-performance binder-free electrode for supercapacitors. *J. Mater. Chem. A* **2015**, *3*, 22081–22087. [CrossRef]

40. Hong, J.; Lee, Y.-W.; Hou, B.; Ko, W.; Lee, J.; Pak, S.; Hong, J.; Morris, S.M.; Cha, S.; Sohn, J.I.; et al. Solubility-Dependent NiMoO$_4$ Nanoarchitectures: Direct Correlation between Rationally Designed Structure and Electrochemical Pseudokinetics. *ACS Appl. Mater. Interfaces* **2016**, *8*, 35227–35234. [CrossRef]

41. Feng, X.; Ning, J.; Wang, D.; Zhang, J.; Xia, M.; Wang, Y.; Hao, Y. Heterostructure arrays of NiMoO$_4$ nanoflakes on N-doping of graphene for high-performance asymmetric supercapacitors. *J. Alloys Compd.* **2020**, *816*, 152625. [CrossRef]

42. Keshari, A.S.; Dubey, P. Rapid microwave-assisted vs. hydrothermal synthesis of hierarchical sheet-like NiO/NiMoO$_4$ hybrid nanostructures for high performance extrinsic pseudocapacitor application. *J. Energy Storage* **2021**, *40*, 102629. [CrossRef]

43. Ajay, A.; Paravannoor, A.; Joseph, J.; Amruthalakshmi, V.; Anoop, S.S.; Nair, S.V.; Balakrishnan, A. 2D amorphous frameworks of NiMoO$_4$ for supercapacitors: Defining the role of surface and bulk controlled diffusion processes. *Appl. Surf. Sci.* **2015**, *326*, 39–47. [CrossRef]

44. Kumbhar, V.S.; Nguyen, V.Q.; Lee, Y.R.; Lokhande, C.D.; Kim, D.-H.; Shim, J.-J. Electrochemically growth-controlled honeycomb-like NiMoO$_4$ nanoporous network on nickel foam and its applications in all-solid-state asymmetric supercapacitors. *New J. Chem.* **2018**, *42*, 14805–14816. [CrossRef]

45. Ho, K.-C.; Lin, L.-Y. A review of electrode materials based on core–shell nanostructures for electrochemical supercapacitors. *J. Mater. Chem. A* **2019**, *7*, 3516–3530. [CrossRef]

46. Ghosh Chaudhuri, R.; Paria, S. Core/shell nanoparticles: Classes, properties, synthesis mechanisms, characterization, and applications. *Chem. Rev.* **2012**, *112*, 2373–2433. [CrossRef] [PubMed]

47. Yuan, J.; Yao, D.; Jiang, L.; Tao, Y.; Che, J.; He, G.; Chen, H. Mn-Doped NiMoO$_4$ Mesoporous Nanorods/Reduced Graphene Oxide Composite for High-Performance All-Solid-State Supercapacitor. *ACS Appl. Energy Mater.* **2020**, *3*, 1794–1803. [CrossRef]

48. Guo, D.; Luo, Y.; Yu, X.; Li, Q.; Wang, T. High performance NiMoO$_4$ nanowires supported on carbon cloth as advanced electrodes for symmetric supercapacitors. *Nano Energy* **2014**, *8*, 174–182. [CrossRef]

49. Zhang, X.; Wei, L.; Guo, X. Ultrathin mesoporous NiMoO$_4$-modified MoO$_3$ core/shell nanostructures: Enhanced capacitive storage and cycling performance for supercapacitors. *Chem. Eng. J.* **2018**, *353*, 615–625. [CrossRef]

50. Yu, D.; Zhang, Z.; Teng, Y.; Meng, Y.; Wu, Y.; Liu, X.; Hua, Y.; Zhao, X.; Liu, X. Fabrication of CuO@NiMoO$_4$ core-shell nanowire arrays on copper foam and their application in high-performance all-solid-state asymmetric supercapacitors. *J. Power Sources* **2019**, *440*, 227164. [CrossRef]

51. Zeng, Y.; Liao, J.; Wei, B.; Huang, Z.; Zhu, W.; Zheng, J.; Liang, H.; Zhang, Y.; Wang, Z. Tuning the electronic structure of NiMoO$_4$ by coupling with SnO$_2$ for high-performance hybrid supercapacitors. *Chem. Eng. J.* **2020**, *409*, 128297. [CrossRef]

52. Guo, D.; Ren, W.; Chen, Z.; Mao, M.; Li, Q.; Wang, T. NiMoO$_4$ nanowire@MnO$_2$ nanoflake core/shell hybrid structure aligned on carbon cloth for high-performance supercapacitors. *RSC Adv.* **2015**, *5*, 10681–10687. [CrossRef]

53. Chen, H.; Yu, L.; Zhang, J.M.; Liu, C.P. Construction of hierarchical NiMoO$_4$@MnO$_2$ nanosheet arrays on titanium mesh for supercapacitor electrodes. *Ceram. Int.* **2016**, *42*, 18058–18063. [CrossRef]

54. Pang, M.; Jiang, S.; Ji, Y.; Zhao, J.; Xing, B.; Pan, Q.; Yang, H.; Qu, W.; Gu, L.; Wang, H. Comparison of α-NiMoO$_4$ nanorods and hierarchical α-NiMoO$_4$@δ-MnO$_2$ core-shell hybrid nanorod/nanosheet aligned on Ni foam for supercapacitors. *J. Alloys Compd.* **2017**, *708*, 14–22. [CrossRef]

55. Wang, X.; Xia, H.; Gao, J.; Shi, B.; Fang, Y.; Shao, M. Enhanced cycle performance of ultraflexible asymmetric supercapacitors based on a hierarchical MnO$_2$@NiMoO$_4$ core–shell nanostructure and porous carbon. *J. Mater. Chem. A* **2016**, *4*, 18181–18187. [CrossRef]

56. Reddy, A.E.; Anitha, T.; Gopi, C.V.V.M.; Rao, S.S.; Kim, H.-J. NiMoO₄@NiWO₄ honeycombs as a high performance electrode material for supercapacitor applications. *Dalton Trans.* **2018**, *47*, 9057–9063. [CrossRef]
57. Hao, J.; Wu, W.; Wang, Q.; Yan, D.; Liu, G.; Peng, S. Effect of grain size on electrochemical performance and kinetics of Co₃O₄ electrode materials. *J. Mater. Chem. A* **2020**, *8*, 7192–7196. [CrossRef]
58. Xuan, H.; Wang, R.; Yang, J.; Zhang, G.; Liang, X.; Li, Y.; Xie, Z.; Han, P. Synthesis of NiMoO₄@Co₃O₄ hierarchical nanostructure arrays on reduced graphene oxide/Ni foam as binder-free electrode for asymmetric supercapacitor. *J. Mater. Sci.* **2021**, *56*, 9419–9433. [CrossRef]
59. Ma, X.-J.; Kong, L.-B.; Zhang, W.-B.; Liu, M.-C.; Luo, Y.-C.; Kang, L. Design and synthesis of 3D Co₃O₄@MMoO₄ (M = Ni, Co) nanocomposites as high-performance supercapacitor electrodes. *Electrochim. Acta* **2014**, *130*, 660–669. [CrossRef]
60. Hong, W.; Wang, J.; Gong, P.; Sun, J.; Niu, L.; Yang, Z.; Wang, Z.; Yang, S. Rational construction of three dimensional hybrid Co₃O₄@NiMoO₄ nanosheets array for energy storage application. *J. Power Sources* **2014**, *270*, 516–525. [CrossRef]
61. Li, Y.; Wang, H.; Jian, J.; Fan, Y.; Yu, L.; Cheng, G.; Zhou, J.; Sun, M. Design of three dimensional hybrid Co₃O₄@NiMoO₄ core/shell arrays grown on carbon cloth as high-performance supercapacitors. *RSC Adv.* **2016**, *6*, 13957–13963. [CrossRef]
62. Zhang, Y.; Yang, Y.; Mao, L.; Cheng, D.; Zhan, Z.; Xiong, J. Growth of three-dimensional hierarchical Co₃O₄@NiMoO₄ core-shell nanoflowers on Ni foam as electrode materials for hybrid supercapacitors. *Mater. Lett.* **2016**, *182*, 298–301. [CrossRef]
63. Yang, F.; Xu, K.; Hu, J. Hierarchical multicomponent electrode with NiMoO₄ nanosheets coated on Co₃O₄ nanowire arrays for enhanced electrochemical properties. *J. Alloys Compd.* **2018**, *781*, 1127–1131. [CrossRef]
64. Zhao, Y.; Zhang, P.; Fu, W.; Ma, X.; Zhou, J.; Zhang, X.; Li, J.; Xie, E.; Pan, X. Understanding the role of Co₃O₄ on stability between active hierarchies and scaffolds: An insight into NiMoO₄ composites for supercapacitors. *Appl. Surf. Sci.* **2017**, *416*, 160–167. [CrossRef]
65. Hu, Q.; Kang, C.; Cao, S.; Zhou, C.; Liu, Q. NiMoO₄ nanosheets grown on MOF-derived leaf-like Co₃O₄ nanosheet arrays for high-performance supercapacitors. *J. Alloys Compd.* **2021**, *883*, 160867. [CrossRef]
66. Dong, T.; Li, M.; Wang, P.; Yang, P. Synthesis of hierarchical tube-like yolk-shell Co₃O₄@NiMoO₄ for enhanced supercapacitor performance. *Int. J. Hydrogen Energy* **2018**, *43*, 14569–14577. [CrossRef]
67. Wang, Y.; Yu, S.; Deng, C.-Y.; Wei, H.-L.; Zhou, J.-H.; Chen, Z.-X.; Yang, H.; Liu, M.-J.; Gu, B.-N.; Chung, C.-C.; et al. Hierarchically Hybrid Porous Co₃O₄@NiMoO₄/CoMoO₄ Heterostructures for High-Performance Electrochemical Energy Storage. *ACS Appl. Mater. Interfaces* **2022**, *14*, 8282–8296. [CrossRef]
68. Zhang, G.; Lou, X.W. General solution growth of mesoporous NiCo₂O₄ nanosheets on various conductive substrates as high-performance electrodes for supercapacitors. *Adv. Mater.* **2012**, *25*, 976–979. [CrossRef]
69. Huang, L.; Chen, D.; Ding, Y.; Feng, S.; Wang, Z.L.; Liu, M. Nickel-cobalt hydroxide nanosheets coated on NiCo₂O₄ nanowires grown on carbon fiber paper for high-performance pseudocapacitors. *Nano Lett.* **2013**, *13*, 3135–3139. [CrossRef]
70. Gong, X.; Cheng, J.; Liu, F.; Zhang, L.; Zhang, X. Nickel–Cobalt hydroxide microspheres electrodepositioned on nickel cobaltite nanowires grown on Ni foam for high-performance pseudocapacitors. *J. Power Sources* **2014**, *267*, 610–616. [CrossRef]
71. Cui, D.; Zhao, R.; Dai, J.; Xiang, J.; Wu, F. A hybrid NiCo₂O₄@NiMoO₄ structure for overall water splitting and excellent hybrid energy storage. *Dalton Trans.* **2020**, *49*, 9668–9679. [CrossRef] [PubMed]
72. Cheng, D.; Yang, Y.; Xie, J.; Fang, C.; Zhang, G.; Xiong, J. Hierarchical NiCo₂O₄@NiMoO₄ core–shell hybrid nanowire/nanosheet arrays for high-performance pseudocapacitors. *J. Mater. Chem. A* **2015**, *3*, 14348–14357. [CrossRef]
73. Gu, Z.; Nan, H.; Geng, B.; Zhang, X. Three-dimensional NiCo₂O₄@NiMoO₄ core/shell nanowires for electrochemical energy storage. *J. Mater. Chem. A* **2015**, *3*, 12069–12075. [CrossRef]
74. Meng, Y.; Liu, J.; Yu, D.; Guo, C.; Liu, L.; Hua, Y.; Wang, C.; Zhao, X.; Liu, X. Design of NiCo₂O₄@NiMoO₄ core–shell nanoarrays on nickel foam to explore the application in both energy storage and electrocatalysis. *Mater. Chem. Front.* **2022**, *6*, 1056–1067. [CrossRef]
75. Xue, W.-D.; Yin, H.; Wang, W.-J.; Zhao, R. Design and Fabrication of Petal-Like NiCo₂O₄@NiMoO₄Core/Shell Nanosheet Arrys Electrode for Asymmetric Supercapacitors. *J. Electrochem. Soc.* **2016**, *164*, A482–A489. [CrossRef]
76. Zhao, H.; Zhang, Z.; Zhou, C.; Zhang, H. Tuning the morphology and size of NiMoO₄ nanosheets anchored on NiCo₂O₄ nanowires: The optimized core-shell hybrid for high energy density asymmetric supercapacitors. *Appl. Surf. Sci.* **2021**, *541*, 148458. [CrossRef]
77. Huang, L.; Zhang, W.; Xiang, J.; Xu, H.; Li, G.; Huang, Y. Hierarchical core-shell NiCo₂O₄@NiMoO₄ nanowires grown on carbon cloth as integrated electrode for high-performance supercapacitors. *Sci. Rep.* **2016**, *6*, 31465. [CrossRef]
78. Hong, W.-L.; Lin, L.-Y. Studying the substrate effects on energy storage abilities of flexible battery supercapacitor hybrids based on nickel cobalt oxide and nickel cobalt oxide@nickel molybdenum oxide. *Electrochim. Acta* **2019**, *308*, 83–90. [CrossRef]
79. Zhang, Q.; Deng, Y.; Hu, Z.; Liu, Y.; Yao, M.; Liu, P. Seaurchin-like hierarchical NiCo₂O₄@NiMoO₄ core–shell nanomaterials for high performance supercapacitors. *Phys. Chem. Chem. Phys.* **2014**, *16*, 23451–23460. [CrossRef]
80. Xue, W.-D.; Wang, W.-J.; Fu, Y.-F.; He, D.-X.; Zeng, F.-Y.; Zhao, R. Rational synthesis of honeycomb-like NiCo₂O₄@NiMoO₄ core/shell nanofilm arrays on Ni foam for high-performance supercapacitors. *Mater. Lett.* **2017**, *186*, 34–37. [CrossRef]
81. Zhang, P.; Zhou, J.; Chen, W.; Zhao, Y.; Mu, X.; Zhang, Z.; Pan, X.; Xie, E. Constructing highly-efficient electron transport channels in the 3D electrode materials for high-rate supercapacitors: The case of NiCo₂O₄@NiMoO₄ hierarchical nanostructures. *Chem. Eng. J.* **2017**, *307*, 687–695. [CrossRef]

82. Zhang, H.; Lu, C.; Hou, H.; Ma, Y.; Yuan, S. Tuning the electrochemical performance of $NiCo_2O_4$@$NiMoO_4$ core-shell heterostructure by controlling the thickness of the $NiMoO_4$ shell. *Chem. Eng. J.* **2019**, *370*, 400–408. [CrossRef]

83. Hong, W.-L.; Lin, L.-Y. Design of nickel cobalt oxide and nickel cobalt oxide@nickel molybdenum oxide battery-type materials for flexible solid-state battery supercapacitor hybrids. *J. Power Sources* **2019**, *435*, 226797. [CrossRef]

84. Kumbhar, V.S.; Lee, W.; Lee, K. Self-assembly of $NiMoO_4$ nanoparticles on the ordered $NiCo_2O_4$ ultra-thin nanoflakes core-shell electrode for high energy density supercapacitors and efficient oxygen evolution reaction. *Ceram. Int.* **2020**, *46*, 22837–22845. [CrossRef]

85. Zhang, M.; Liu, W.; Han, R.; Xu, J.; Sun, Z.; Liu, J.; Wu, Y. Facile Construction of 3D Packing Porous Flower-Like $NiCo_2O_4$@$NiMoO_4$/rGO Hybrids as High-Performance Supercapacitors with Large Areal Capacitance. *Energy Technol.* **2018**, *7*, 1800940. [CrossRef]

86. Yedluri, A.K.; Kim, H.-J. Wearable super-high specific performance supercapacitors using a honeycomb with folded silk-like composite of $NiCo_2O_4$ nanoplates decorated with $NiMoO_4$ honeycombs on nickel foam. *Dalton Trans.* **2018**, *47*, 15545–15554. [CrossRef]

87. Wang, Z.; Lu, S.; He, G.; Lv, A.; Shen, Y.; Xu, W. In situ construction of dual-morphology $ZnCo_2O_4$ for high-performance asymmetric supercapacitors. *Nanoscale Adv.* **2019**, *1*, 3086–3094. [CrossRef]

88. Chen, C.; Wang, S.; Luo, X.; Gao, W.; Huang, G.; Zeng, Y.; Zhu, Z. Reduced $ZnCo_2O_4$@$NiMoO_4 \cdot H_2O$ heterostructure electrodes with modulating oxygen vacancies for enhanced aqueous asymmetric supercapacitors. *J. Power Sources* **2019**, *409*, 112–122. [CrossRef]

89. Hong, J.; Lee, Y.-W.; Ahn, D.; Pak, S.; Lee, J.; Jang, A.-R.; Lee, S.; Hou, B.; Cho, Y.; Morris, S.M.; et al. Highly stable 3D porous heterostructures with hierarchically-coordinated octahedral transition metals for enhanced performance supercapacitors. *Nano Energy* **2017**, *39*, 337–345. [CrossRef]

90. Wang, J.; Wang, S.; Tian, Y.; Jin, X.; Dong, J. 3D heterogeneous $ZnCo_2O_4$@$NiMoO_4$ nanoarrays grown on Ni foam as a binder-free electrode for high-performance energy storage. *J. Energy Storage* **2020**, *32*, 101899. [CrossRef]

91. Meng, Y.; Yu, D.; Teng, Y.; Qi, H.; Liu, X.; Wu, Y.; Zhao, X.; Liu, X. Coating of the $NiMoO_4$ nanosheets on different-morphology $ZnCo_2O_4$ nanoarrays on Ni foam and their application in battery-supercapacitor hybrid devices. *J. Energy Storage* **2020**, *29*, 101195. [CrossRef]

92. Lin, J.; Liang, H.; Jia, H.; Chen, S.; Cai, Y.; Qi, J.; Cao, J.; Fei, W.; Feng, J. Hierarchical $CuCo_2O_4$@$NiMoO_4$ core–shell hybrid arrays as a battery-like electrode for supercapacitors. *Inorg. Chem. Front.* **2017**, *4*, 1575–1581. [CrossRef]

93. Li, G.; Song, B.; Cui, X.; Ouyang, H.; Wang, K.; Sun, Y.; Wang, Y. Multidimensional and Binary Micro $CuCo_2O_4$/Nano $NiMoO_4$ for High-Performance Supercapacitors. *ACS Sustain. Chem. Eng.* **2020**, *8*, 1687–1694. [CrossRef]

94. Mehrez, J.A.-A.; Owusu, K.A.; Chen, Q.; Li, L.; Hamwi, K.; Luo, W.; Mai, L. Hierarchical $MnCo_2O_4$@$NiMoO_4$ as free-standing core–shell nanowire arrays with synergistic effect for enhanced supercapacitor performance. *Inorg. Chem. Front.* **2019**, *6*, 857–865. [CrossRef]

95. Chen, T.; Shi, R.; Zhang, Y.; Wang, Z. A $MnCo_2O_4$@$NiMoO_4$Core-Shell Composite Supported on Nickel Foam as a Supercapacitor Electrode for Energy Storage. *ChemPlusChem* **2019**, *84*, 69–77. [CrossRef] [PubMed]

96. Gao, H.; Wang, X.; Wang, G.; Hao, C.; Huang, C.; Jiang, C. Facile construction of a $MgCo_2O_4$@$NiMoO_4$/NF core–shell nanocomposite for high-performance asymmetric supercapacitors. *J. Mater. Chem. C* **2019**, *7*, 13267–13278. [CrossRef]

97. Teng, Y.; Yu, D.; Li, Y.; Meng, Y.; Xue, Y.; Liu, J.; Feng, Y.; Wang, C.; Hua, Y.; Zhao, X.; et al. Facile Synthesis of $MgCo_2O_4$@$MMoO_4$ (M = Co, Ni) Nanosheet Arrays on Nickel Foam as an Advanced Electrode for Asymmetric Supercapacitors. *Energy Fuels* **2021**, *35*, 6272–6281. [CrossRef]

98. Tang, X.; Lui, Y.H.; Zhang, B.; Hu, S. Venus flytrap-like hierarchical NiCoMn–O@$NiMoO_4$@C nanosheet arrays as free-standing core-shell electrode material for hybrid supercapacitor with high electrochemical performance. *J. Power Sources* **2020**, *477*, 228977. [CrossRef]

99. Bandyopadhyay, P.; Saeed, G.; Kim, N.H.; Lee, J.H. Zinc-nickel-cobalt oxide@$NiMoO_4$ core-shell nanowire/nanosheet arrays for solid state asymmetric supercapacitors. *Chem. Eng. J.* **2020**, *384*, 123357. [CrossRef]

100. Wang, J.; Zhang, L.; Liu, X.; Zhang, X.; Tian, Y.; Liu, X.; Zhao, J.; Li, Y. Assembly of flexible $CoMoO_4$@$NiMoO_4 \cdot xH_2O$ and Fe_2O_3 electrodes for solid-state asymmetric supercapacitors. *Sci. Rep.* **2017**, *7*, 41088. [CrossRef]

101. Liu, M.-C.; Kong, L.-B.; Lu, C.; Ma, X.-J.; Li, X.-M.; Luo, Y.-C.; Kang, L. Design and synthesis of $CoMoO_4$–$NiMoO_4 \cdot xH_2O$ bundles with improved electrochemical properties for supercapacitors. *J. Mater. Chem. A* **2013**, *1*, 1380–1387. [CrossRef]

102. Zhang, Z.; Zhang, H.; Zhang, X.; Yu, D.; Ji, Y.; Sun, Q.; Wang, Y.; Liu, X. Facile synthesis of hierarchical $CoMoO_4$@$NiMoO_4$ core–shell nanosheet arrays on nickel foam as an advanced electrode for asymmetric supercapacitors. *J. Mater. Chem. A* **2016**, *4*, 18578–18584. [CrossRef]

103. Nti, F.; Anang, D.A.; Han, J.I. Facilely synthesized $NiMoO_4$/$CoMoO_4$ nanorods as electrode material for high performance supercapacitor. *J. Alloys Compd.* **2018**, *742*, 342–350. [CrossRef]

104. Zhang, P.; Zhang, X.; Li, G. Fabrication of rod-like $NiMoO_4$/$CoMoO_4$ for application in asymmetric supercapacitors. *Ionics* **2020**, *26*, 393–401. [CrossRef]

105. Chen, S.; Chandrasekaran, S.; Cui, S.; Li, Z.; Deng, G.; Deng, L. Self-supported $NiMoO_4$@$CoMoO_4$ core/sheath nanowires on conductive substrates for all-solid-state asymmetric supercapacitors. *J. Electroanal. Chem.* **2019**, *846*, 113153. [CrossRef]

106. Hu, B.; Cen, Y.; Xu, C.; Xiang, Q.; Aslam, M.K.; Liu, L.; Li, S.; Liu, Y.; Yu, D.; Chen, C. Hierarchical NiMoO$_4$@Co$_3$V$_2$O$_8$ hybrid nanorod/nanosphere clusters as advanced electrodes for high-performance electrochemical energy storage. *Nanoscale* **2020**, *12*, 3763–3776. [CrossRef]

107. Sharma, P.; Sundaram, M.M.; Watcharatharapong, T.; Jungthawan, S.; Ahuja, R. Tuning the Nanoparticle Interfacial Properties and Stability of the Core–Shell Structure in Zn-Doped NiMoO$_4$@AWO$_4$. *ACS Appl. Mater. Interfaces* **2021**, *13*, 56116–56130. [CrossRef]

108. Acharya, J.; Pant, B.; Ojha, G.P.; Park, M. Embellishing hierarchical 3D core-shell nanosheet arrays of ZnFe$_2$O$_4$@NiMoO$_4$ onto rGO-Ni foam as a binder-free electrode for asymmetric supercapacitors with excellent electrochemical performance. *J. Colloid Interface Sci.* **2022**, *610*, 863–878. [CrossRef]

109. Dong, J.Y.; Xu, J.C.; Hui, K.N.; Yang, Y.; Su, S.C.; Li, L.; Zhang, X.T.; Ng, K.W.; Wang, S.P.; Tang, Z.K. Homogeneous Core/Shell NiMoO$_4$@NiMoO$_4$ and Activated Carbon for High Performance Asymmetric Supercapacitor. *Nanomaterials* **2019**, *9*, 1033. [CrossRef]

110. Chen, S.; Zhang, M.; Jiang, G.; Zhang, Z.; Zhou, X. NiMoO$_4$ nanorods@hydrous NiMoO$_4$ nanosheets core-shell structured arrays for pseudocapacitor application. *J. Alloys Compd.* **2019**, *814*, 152253. [CrossRef]

111. Lang, J.-W.; Kong, L.-B.; Liu, M.; Luo, Y.-C.; Kang, L. Co$_{0.56}$Ni$_{0.44}$ Oxide Nanoflake Materials and Activated Carbon for Asymmetric Supercapacitor. *J. Electrochem. Soc.* **2010**, *157*, A1341–A1346. [CrossRef]

112. Owusu, K.A.; Qu, L.; Li, J.; Wang, Z.; Zhao, K.; Yang, C.; Hercule, K.M.; Lin, C.; Shi, C.; Wei, Q.; et al. Low-crystalline iron oxide hydroxide nanoparticle anode for high-performance supercapacitors. *Nat. Commun.* **2017**, *8*, 14264. [CrossRef] [PubMed]

113. Jiang, G.; Zhang, M.; Li, X.; Gao, H. NiMoO$_4$@Ni(OH)$_2$ core/shell nanorods supported on Ni foam for high-performance supercapacitors. *RSC Adv.* **2015**, *5*, 69365–69370. [CrossRef]

114. Ren, W.; Guo, D.; Zhuo, M.; Guan, B.; Zhang, D.; Li, Q. NiMoO$_4$@Co(OH)$_2$ core/shell structure nanowire arrays supported on Ni foam for high-performance supercapacitors. *RSC Adv.* **2015**, *5*, 21881–21887. [CrossRef]

115. Yan, L.; Chen, X. Nanomaterials for Drug Delivery. In *Nanocrystalline Materials*, 2nd ed.; Tjong, S.C., Ed.; Elsevier Ltd.: Amsterdam, The Netherlands, 2013; pp. 221–268. [CrossRef]

116. Jiang, M.; Zhang, X. Carbon fiber/Ni-Co layered double hydroxide@NiMoO$_4$/graphene oxide sandwich structure flexible electrode materials: Facile synthesis and high supercapacitor performance. *J. Alloys Compd.* **2019**, *794*, 13–20. [CrossRef]

117. Hu, C.; Gong, J.; Wang, J.; Zhou, T.; Xie, M.; Wang, S.; Dai, Y. Composites of NiMoO$_4$@Ni-Co LDH@NiCo$_2$O$_4$ on Ni foam with a rational microscopic morphology for high-performance asymmetric supercapacitors. *J. Alloys Compd.* **2022**, *902*, 163749. [CrossRef]

118. Zhu, Z.; Tian, W.; Lv, X.; Wang, F.; Hu, Z.; Ma, K.; Wang, C.; Yang, T.; Ji, J. P-doped cobalt carbonate hydroxide@NiMoO$_4$ double-shelled hierarchical nanoarrays anchored on nickel foam as a bi-functional electrode for energy storage and conversion. *J. Colloid Interface Sci.* **2020**, *587*, 855–863. [CrossRef]

119. Gao, Y.; Zhao, L. Review on recent advances in nanostructured transition-metal-sulfide-based electrode materials for cathode materials of asymmetric supercapacitors. *Chem. Eng. J.* **2022**, *430*, 132745. [CrossRef]

120. Lu, L.; Xu, Q.; Chen, Y.; Zhou, Y.; Jiang, T.; Zhao, Q. Preparation of metal sulfide electrode materials derived based on metal organic framework and application of supercapacitors. *J. Energy Storage* **2022**, *49*, 104073. [CrossRef]

121. Yu, Z.; Zhang, N.; Li, G.; Ma, L.; Li, T.; Tong, Z.; Li, Y.; Wang, K. Funnel-shaped hierarchical NiMoO$_4$@Co$_3$S$_4$ core-shell nanostructure for enhanced supercapacitor performance. *J. Energy Storage* **2022**, *51*, 104511. [CrossRef]

122. Wan, L.; Liu, J.; Li, X.; Zhang, Y.; Chen, J.; Du, C.; Xie, M. Fabrication of core-shell NiMoO$_4$@MoS$_2$ nanorods for high-performance asymmetric hybrid supercapacitors. *Int. J. Hydrogen Energy* **2020**, *45*, 4521–4533. [CrossRef]

123. Yu, B.; Jiang, G.; Xu, W.; Cao, C.; Liu, Y.; Lei, N.; Evariste, U.; Ma, P. Construction of NiMoO$_4$/CoMoO$_4$ nanorod arrays wrapped by Ni-Co-S nanosheets on carbon cloth as high performance electrode for supercapacitor. *J. Alloys Compd.* **2019**, *799*, 415–424. [CrossRef]

124. Xing, B.; Zhao, J.; Jiang, S.; Pang, M.; Pan, Q.; Geng, Y.; Ma, G.; Li, Z.; Han, P. NiMoO$_4$@Ni$_3$S$_2$ core-shell composites grown in situ on nickel foam for applications in supercapacitors. *Synth. Met.* **2020**, *271*, 116638. [CrossRef]

125. Chen, F.; Ji, S.; Liu, Q.; Wang, H.; Liu, H.; Brett, D.J.L.; Wang, G.; Wang, R. Rational Design of Hierarchically Core-Shell Structured Ni$_3$S$_2$@NiMoO$_4$ Nanowires for Electrochemical Energy Storage. *Small* **2018**, *14*, e1800791. [CrossRef] [PubMed]

126. Chen, D.; Lu, M.; Li, L.; Cai, D.; Li, J.; Cao, J.; Han, W. Hierarchical core–shell structural NiMoO$_4$@NiS$_2$/MoS$_2$ nanowires fabricated via an in situ sulfurization method for high performance asymmetric supercapacitors. *J. Mater. Chem. A* **2019**, *7*, 21759–21765. [CrossRef]

127. Chen, L.; Deng, W.; Chen, Z.; Wang, X. Hetero-architectured core–shell NiMoO$_4$@Ni$_9$S$_8$/MoS$_2$ nanorods enabling high-performance supercapacitors. *J. Mater. Res.* **2021**, *37*, 284–293. [CrossRef] [PubMed]

128. Wang, Y.; Li, H.; Ren, Y.; Chen, X.; Xie, K.; Sun, Y. Nanowire-core/double-shell of NiMoO$_4$@C@Ni$_3$S$_2$ arrays on Ni foam: Insights into supercapacitive performance and capacitance degradation. *Nanotechnology* **2018**, *29*, 385402. [CrossRef]

129. Xing, T.; Ouyang, Y.; Chen, Y.; Zheng, L.; Shu, H.; Wu, C.; Chang, B.; Wang, X. Preparation and performances of 3D hierarchical core-shell structural NiCo$_2$S$_4$@NiMoO$_4$xH$_2$O nanoneedles for electrochemical energy storage. *Electrochim. Acta* **2020**, *351*, 136447. [CrossRef]

130. Chen, S.; Zhang, Z.; Zeng, W.; Chen, J.; Deng, L. Construction of NiCo$_2$S$_4$@NiMoO$_4$ Core-Shell Nanosheet Arrays with Superior Electrochemical Performance for Asymmetric Supercapacitors. *ChemElectroChem* **2019**, *6*, 590–597. [CrossRef]

131. Zhang, Y.; Xu, J.; Zheng, Y.; Zhang, Y.; Hu, X.; Xu, T. NiCo$_2$S$_4$@NiMoO$_4$ Core-Shell Heterostructure Nanotube Arrays Grown on Ni Foam as a Binder-Free Electrode Displayed High Electrochemical Performance with High Capacity. *Nanoscale Res. Lett.* **2017**, *12*, 412. [CrossRef]

132. Yao, M.; Hu, Z.; Liu, Y.; Liu, P. Design and synthesis of hierarchical NiCo$_2$S$_4$@NiMoO$_4$core/shell nanospheres for high-performance supercapacitors. *New J. Chem.* **2015**, *39*, 8430–8438. [CrossRef]

133. Wang, P.; Cai, H.; Li, X.; Yang, Y.; Li, G.; Xie, J.; Xia, H.; Sun, P.; Zhang, D.; Xiong, J. Construction of hierarchical NiCo$_2$S$_4$ nanotube@NiMoO$_4$ nanosheet hybrid arrays as advanced battery-type electrodes for hybrid supercapacitors. *New J. Chem.* **2019**, *43*, 7065–7073. [CrossRef]

134. Chiu, K.-L.; Lin, L.-Y. Applied potential-dependent performance of the nickel cobalt oxysulfide nanotube/nickel molybdenum oxide nanosheet core–shell structure in energy storage and oxygen evolution. *J. Mater. Chem. A* **2019**, *7*, 4626–4639. [CrossRef]

135. Chen, C.; Yan, D.; Luo, X.; Gao, W.; Huang, G.; Han, Z.; Zeng, Y.; Zhu, Z. Construction of Core–Shell NiMoO$_4$@Ni-Co-S Nanorods as Advanced Electrodes for High-Performance Asymmetric Supercapacitors. *ACS Appl. Mater. Interfaces* **2018**, *10*, 4662–4671. [CrossRef] [PubMed]

136. Acharya, J.; Ojha, G.P.; Kim, B.-S.; Pant, B.; Park, M. Modish Designation of Hollow-Tubular rGO–NiMoO$_4$@Ni–Co–S Hybrid Core–shell Electrodes with Multichannel Superconductive Pathways for High-Performance Asymmetric Supercapacitors. *ACS Appl. Mater. Interfaces* **2021**, *13*, 17487–17500. [CrossRef] [PubMed]

137. Acharya, J.; Pant, B.; Ojha, G.P.; Park, M. Unlocking the potential of a novel hierarchical hybrid (Ni–Co)Se$_2$@NiMoO$_4$@rGO–NF core–shell electrode for high-performance hybrid supercapacitors. *J. Mater. Chem. A* **2022**, *10*, 7999–8014. [CrossRef]

138. Gao, M.; Le, K.; Xu, D.; Wang, Z.; Wang, F.; Liu, W.; Yu, H.; Liu, J.; Chen, C. Controlled sulfidation towards achieving core-shell 1D-NiMoO$_4$@2D-NiMoS$_4$ architecture for high-performance asymmetric supercapacitor. *J. Alloys Compd.* **2019**, *804*, 27–34. [CrossRef]

139. Wei, C.; Huang, Y.; Yan, J.; Chen, X.; Zhang, X. Synthesis of hierarchical carbon sphere@NiMoO$_4$ composite materials for supercapacitor electrodes. *Ceram. Int.* **2016**, *42*, 15694–15700. [CrossRef]

140. Teng, C.; Gao, X.; Zhang, N.; Jia, Y.; Li, X.; Shi, Z.; Wu, Z.; Zhi, M.; Hong, Z. Synthesis of coaxial carbon@NiMoO$_4$ composite nanofibers for supercapacitor electrodes. *RSC Adv.* **2018**, *8*, 32979–32984. [CrossRef]

141. Zheng, Y.; Xu, J.; Zhang, Y.; Yang, X.; Zhang, Y.; Shang, Y. Nitrogen-doped carbon nanotube supported double-shelled hollow composites for asymmetric supercapacitors. *New J. Chem.* **2018**, *42*, 150–160. [CrossRef]

142. Yan, T.; Wang, M.; Li, K.; Ni, X.; Du, X.; Xi, M.; Chen, H.; Ju, A. Freestanding XMoO$_4$ nanosheet arrays@hollow porous carbon submicrofiber composites for flexible all-solid-state symmetric supercapacitors. *J. Alloys Compd.* **2021**, *898*, 162834. [CrossRef]

143. Yao, P.; Li, C.; Yu, J.; Zhang, S.; Zhang, M.; Liu, H.; Ji, M.; Cong, G.; Zhang, T.; Zhu, C.; et al. High performance flexible energy storage device based on copper foam supported NiMoO$_4$ nanosheets-CNTs-CuO nanowires composites with core–shell holey nanostructure. *J. Mater. Sci. Technol.* **2021**, *85*, 87–94. [CrossRef]

144. Chen, T.; Xiang, C.; Zou, Y.; Xu, F.; Sun, L. All-Solid High-Performance Asymmetric Supercapacitor Based on Yolk–Shell NiMoO$_4$/V$_2$CT$_x$@Reduced Graphene Oxide and Hierarchical Bamboo-Shaped MoO$_2$@Fe$_2$O$_3$/N-Doped Carbon. *Energy Fuels* **2021**, *35*, 10250–10261. [CrossRef]

145. Gao, H.; Wu, F.; Wang, X.; Hao, C.; Ge, C. Preparation of NiMoO$_4$-PANI core-shell nanocomposite for the high-performance all-solid-state asymmetric supercapacitor. *Int. J. Hydrogen Energy* **2018**, *43*, 18349–18362. [CrossRef]

146. Zhu, D.; Sun, X.; Yu, J.; Liu, Q.; Liu, J.; Chen, R.; Zhang, H.; Song, D.; Li, R.; Wang, J. Three-dimensional heterostructured polypyrrole/nickel molybdate anchored on carbon cloth for high-performance flexible supercapacitors. *J. Colloid Interface Sci.* **2020**, *574*, 355–363. [CrossRef]

147. Shen, J.; Wang, Q.; Zhang, K.; Wang, S.; Li, L.; Dong, S.; Zhao, S.; Chen, J.; Sun, R.; Wang, Y.; et al. Flexible carbon cloth based solid-state supercapacitor from hierarchical holothurian-morphological NiCo$_2$O$_4$@NiMoO$_4$/PANI. *Electrochim. Acta* **2019**, *320*, 134578. [CrossRef]

148. Yi, T.-F.; Qiu, L.-Y.; Mei, J.; Qi, S.-Y.; Cui, P.; Luo, S.; Zhu, Y.-R.; Xie, Y.; He, Y.-B. Porous spherical NiO@NiMoO$_4$@PPy nanoarchitectures as advanced electrochemical pseudocapacitor materials. *Sci. Bull.* **2020**, *65*, 546–556. [CrossRef]

149. Wang, Y.; Sun, J.; Qian, X.; Zhang, Y.; Yu, L.; Niu, R.; Zhao, H.; Zhu, J. 2D/2D heterostructures of nickel molybdate and MXene with strong coupled synergistic effect towards enhanced supercapacitor performance. *J. Power Sources* **2019**, *414*, 540–546. [CrossRef]